






Hall effect and symmetry breaking in the nonmagnetic metal LuB₁₂ with dynamic charge stripesN. Sluchanko ^{1,*}, A. Azarevich ¹, A. Bogach,¹ S. Demishev,¹ K. Krasikov,¹ V. Voronov ¹, V. Filipov,² N. Shitsevalova ² and V. Glushkov¹¹*Prokhorov General Physics Institute of the Russian Academy of Sciences, 38 Vavilov Str., 119991 Moscow, Russia*²*Frantsevich Institute for Problems of Materials Science, National Academy of Sciences of Ukraine,**3 Krzhizhanovsky Str., 03680 Kyiv, Ukraine* (Received 4 August 2020; revised 30 October 2020; accepted 18 December 2020; published 13 January 2021)

A comprehensive study of magnetoresistance and Hall effect has been performed for the set of the single crystals of nonmagnetic metal LuB₁₂ with the Jahn-Teller instability of the boron cage and dynamic charge stripes forming along ⟨110⟩ direction. An anomalous positive contribution to Hall effect for a particular direction of magnetic field $\mathbf{H}/[001]$ is found in the single crystals of LuB₁₂ of the highest quality. This contribution arising at $T_E \sim 150$ K is shown to increase drastically when approaching the disordered ground state below $T^* \sim 60$ K. The Hall effect anomaly is shown to appear in combination with the peak of magnetoresistance. The various scenarios allowing for the topology of Fermi surface, anisotropy of relaxation time for charge carriers, and interaction of external magnetic field with the filamentary structure of fluctuating charge stripes are analyzed to explain the features of magnetotransport in this metal with inhomogeneous distribution of electron density. The origin of SdH oscillations, which are observed in this nonequilibrium metal with electron phase separation and strong charge carrier scattering, is discussed.

DOI: [10.1103/PhysRevB.103.035117](https://doi.org/10.1103/PhysRevB.103.035117)**I. INTRODUCTION**

The unique opportunity for studying of the features of electron phase separation in strongly correlated electron systems is provided by dynamic or fluctuating charge and spin stripes, which attract extraordinary scientific interest due to their important role in the mechanism of high temperature superconductivity (HTSC, see, e.g., [1–14]). While the stripe states are generally considered as a special feature for the La_{2-x}Ba_xCuO₄ perovskite family [15], phase singularities accompanied by lowered symmetry of the lattice are detected in other cuprates (YBa₂Cu₃O_{7-δ} [16,17], SmBa₂Cu₃O_x [18], Bi₂Sr₂CaCu₂O_{8+δ} [19], and Ca_{2-x}Na_xCuO₂Cl₂ [20]). This kind of electron instability is also suggested to be extremely important for the understanding of exotic physics in colossal magnetoresistive manganites [21,22], nickelates [23–25], iron-based superconductors [26,27], heavy fermion hexaborides [28], etc.

A special kind of fluctuating charge stripes have been recently detected in the nonmagnetic dodecaboride LuB₁₂ [29–31] with an exceptionally high diffraction quality of crystals (worldwide record of structure refinement factor [32]) and in magnetic Tm_{1-x}Yb_xB₁₂ compounds with a metal-insulator transition [33]. The mechanism responsible for this electron and lattice instability in RB₁₂ with fcc crystal structure is related to dynamic cooperative Jahn-Teller (JT) effect in the B₁₂ clusters [29,31]. It was shown in [29] that, because of triple orbital degeneracy of the ground electronic state, the isolated cubo-octahedral boron clusters [B₁₂]ⁿ⁻ ($n = 0-4$) are

JT active and their structure is labile due to JT distortions. The quantum chemical calculations and geometry optimizations for the charged cubo-octahedral [B₁₂]²⁻ cluster, whose doubly negative charge state is regarded as the most relevant one in RB₁₂ compounds [29], allow us to conclude in favor of trigonal and tetragonal distortions and mixture via a nonadiabatic electron-vibronic coupling of electronic states for each B₁₂ cluster [34]. In the dodecaboride matrix [see fragment of the fcc crystal structure in Fig. 1(a)], the *collective JT effect* in the lattice of these cubo-octahedral B₁₂ complexes is the origin of both the collective dynamics of boron clusters and large amplitude vibrations (rattling modes) of the rare earth ions embedded in B₂₄ cavities of the boron cage [see Fig. 1(b)]. In accord with this conclusions [35,36], the collective JT dynamics of the cubo-octahedral clusters [B₁₂]²⁻ arises due to the ferrodistorive effect developed in the rigid boron sublattice of RB₁₂ (see also Fig. S13 in [37] for more detail). Strong coupling of these Lu rattling modes located at 110 cm⁻¹ (~ 14 meV) [38] and the JT active vibrations of boron are the origin of both lattice instability and the emergence of the collective excitations in the optical spectra of LuB₁₂ [39].

The Lu rattling modes correspond to Einstein oscillators in the double-well potential [Fig. 1(c)]. The large amplitude of these rattling modes initiates strong changes in the *hybridization* of rare earth and boron electron states (see Fig. S13 in [37]). Since the states in the conduction band are contributed by the 2*p* orbitals of B₁₂ and the 5*d* orbitals of Lu [40–43], the variation of the 5*d*-2*p* hybridization leads to the modulation of conduction bandwidth and, consequently, may generate nonequilibrium (“hot”) electron states. These charge carriers seem to amount to $\sim 70\%$ from the total number of conduction

*Corresponding author: nes@lt.gpi.ru

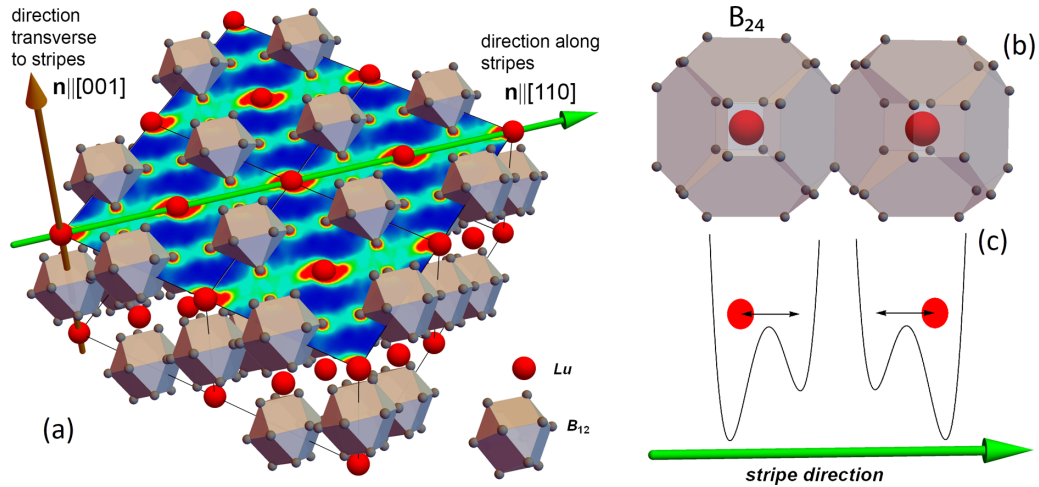


FIG. 1. (a) Crystal structure of RB₁₂. Color plane shows the map of the electron density in the face (001) obtained by the maximum entropy method (MEM) [30]. Green bars correspond to the dynamic charge stripes. Directions along ($\mathbf{n}/[110]$) and transverse ($\mathbf{n}/[001]$) to the stripes are shown. (b) Fragment of the crystal structure demonstrates two connected B₂₄ clusters with embedded Lu³⁺ ions. (c) The schematic view of two double-well potentials for neighboring Lu ions.

electrons as estimated from overdamped oscillators in the optical conductivity spectra at room temperature [39]. Due to the stripe formation, a considerable number of nonequilibrium conduction electrons are accumulated in the filamentary structure of fluctuating charges (see the wide green channels in Fig. 1(a) [30]). Note also that the lattice and electron systems of LuB₁₂ are significantly modified below $T^* \sim 60$ K where the cage-glass state [44] is formed due to positional disorder of the loosely bound Lu³⁺ ions embedded in B₂₄ truncated cubo-octahedrons caused by static displacements of R³⁺ ions in the double-well potential [Figs. 1(b) and 1(c)].

The investigation of crystal structure, heat capacity, and charge transport [31] allowed us to argue that in the family of Lu^NB₁₂ crystals with various boron isotopes $N = 10, 11$, nat (the last index corresponds to the natural mixture of 18.8% ¹⁰B and 81.2% ¹¹B) Lu^{nat}B₁₂ possesses the strongest local atomic disordering in combination with long-range JT trigonal distortions. These factors provide optimal conditions for the formation of the dynamic charge stripes below $T^* \sim 60$ K. As a result, the resistivity and Seebeck coefficient of the Lu^{nat}B₁₂ heterogeneous medium decrease strongly in comparison with those detected for pure boron isotope crystals. It was concluded in [31] that any defects are supposedly used as the pinning centers facilitating the formation of additional quantum conductive channels (dynamic charge stripes) in the metallic matrix of RB₁₂.

Hall effect is usually considered as a key experiment to reveal a transformation of electron spectrum in the vicinity of a quantum critical point (QCP) [45–48], in the stripe-ordered compounds [49,50], near the metal-insulator transition [51–53], etc. All the singularities were detected in the Tm_{1-x}Yb_xB₁₂ family [33,54] and the complicated behavior of the Hall resistivity components was interpreted in terms of both the metal-insulator transition and electron phase separation effects in combination with the formation of nanoclusters of the rare earth ions in the cage-glass state of the studied compounds. The instability of Yb 4*f*-electron configuration in these Yb-based rare-earth dodecaborides is

developed in combination with the JT deformations of the boron cage (Yb ion valence is about 2.92–2.95 [55,56]). This phenomenon provides one more mechanism of the charge and spin fluctuations in RB₁₂ and it is promising to separate only the influence of dynamic charge stripes on the Hall voltage anomalies in RB₁₂. In this study we present the results of detailed Hall effect measurements of different quality single crystals of the nonmagnetic reference compound LuB₁₂. We show here that an ordinary Hall effect in LuB₁₂ is modified by the appearance of a specific contribution to the Hall resistivity, which could not be explained exclusively in terms of anisotropic Fermi surface and is suggested to be caused by an interaction of the dynamic charge stripes with external magnetic field.

II. EXPERIMENTAL DETAILS

A. Crystal growth

The single crystals of nonmagnetic LuB₁₂ dodecaboride were grown using the induction crucible-free zone melting method with multiple remelting in an argon gas atmosphere from the preliminarily synthesized LuB₁₂ powders [57]. All the crystals under investigation (samples 1–6) have been grown from the initial high purity LuB₁₂ powder synthesized from the 4N lutetium oxide Lu₂O₃ (99.9985 wt.% purity, particle size less than 100 μm) and 3N amorphous boron (99.9 wt.% purity, particle size about 50 Å). The details of both ingot preparation and solid state reaction are given in [37]. Different technological regimes were applied during the growing process. In the case of crystal 1, an additional purification of argon from possible contamination of other gases was carried out directly in the growth chamber where Ti was used as a getter. Crystals 1 and 2 and 4–6 were grown with single zone passing under different pressures of argon gas ranging from 0.15 to 0.5 MPa with equal crystallization rates. Crystal 3, with the highest residual resistivity value, was grown with triple zone passing (see [37] for more details).

Perfect x-ray diffraction reflexes in Laue pattern (for crystals 1–6) and quantum oscillations of the magnetization (de Haas–van Alphen effect) observed in magnetic field $\mathbf{H} // [100]$ (for crystal 1) prove the high quality of the crystals under investigation. Note that previous results of high precision x-ray diffraction measurements of the single-domain crystals 1 and 2 of LuB_{12} [29–32] allow us to conclude about the exceptionally high diffraction quality of these samples (worldwide record of the structure refinement factor [32]).

B. Galvanomagnetic measurements

The samples for magnetoresistance (MR) and Hall effect (HE) measurements were cut from the single domain crystals oriented along the principal crystallographic directions with accuracy $\sim 2^\circ$, then these were polished and etched to delete the distorted surface layer. The angular dependencies of resistivity and Hall voltage were measured by the original sample rotation technique with a stepwise ($\Delta\varphi = 1.8^\circ$) fixing of the sample position in the steady magnetic field. The magnetic field supplied by the superconducting solenoid up to 80 kOe was applied perpendicular to the measuring direct current (DC) $\mathbf{I} // (110)$ in 1–6 [see inset in Fig. 5(a) below, the orientation of the normal vector $\mathbf{n} // (001)$, or $\mathbf{n} // (110)$ was used]. For sample 1 the resistivity and Hall effect measurements were carried out also in the magnetic field up to 140 kOe at liquid helium temperature (sample 1a, $\mathbf{I} // [110]$) and for 1 and 2 in various DC directions (samples 1b and 1c with $\mathbf{I} // [100]$ and $\mathbf{I} // [010]$, correspondingly). The installation equipped with a step motor with automated control of the step-by-step sample rotation is similar to the one applied previously in [54]. High accuracy of the temperature control ($\Delta T \approx 0.002$ K in the range 1.8–7 K) and magnetic field stabilization ($\Delta H \approx 2$ Oe) was achieved by using the commercial temperature controller TC 1.5/300 and superconducting magnet power supply unit SMPS 100 (Cryotel Ltd.) in combination with the CERNOX 1050 thermometer (Lake Shore Cryotronics, Inc.) and Hall sensors.

III. EXPERIMENTAL RESULTS AND ANALYSIS

A. Temperature dependencies ($\mathbf{I} // (110)$)

Figure 2 shows the metallic type temperature dependencies of resistivity $\rho(T)$ measured for various LuB_{12} single crystals. The temperature independent “plateau” is observed on the $\rho(T)$ curves in the range $T \leq 20$ K for all the studied crystals. The residual resistivity ratio [RRR = $\rho(300 \text{ K})/\rho(4.2 \text{ K})$] varies about by the factor 6 from ~ 70 (sample 1) to ~ 12 (sample 3). The resistivity $\rho(T, H_0)$ and the reduced Hall resistivity $\rho_H/H = f(T, H_0)$ have been studied in detail in magnetic field $H_0 = 80$ kOe for samples 1, 2, and 3 in two orientations $\mathbf{H} // [100]$ and $\mathbf{H} // [110]$ (see Fig. 3). Taking into account the electron density inhomogeneity in LuB_{12} due to dynamic charge stripes found in the dodecaboride matrix [30] [see Fig. 1(a)], the term “reduced Hall resistivity” $\rho_H/H = f(T, H_0)$ will be used below instead of Hall coefficient $R_H(T, H_0) \equiv \rho_{xy}/H$. Figure 3 presents the data of Hall resistivity measured for two opposite directions of external magnetic field $\pm \mathbf{H} // \mathbf{n}$ and calculated applying the

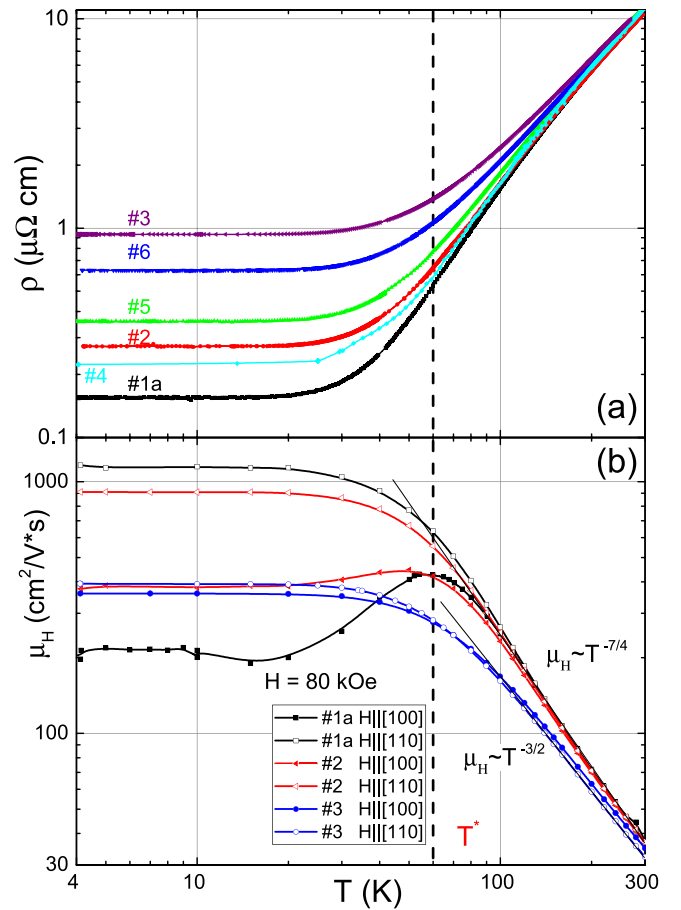


FIG. 2. Temperature dependencies of (a) the resistivity and (b) Hall mobility at $H = 80$ kOe of the LuB_{12} crystals. Vertical dashed line marks the transition at $T^* \sim 60$ K to the cage-glass state.

general relation $\rho_H = \{[V_H(H) - V_H(-H)]/(2I)\}d$ (V_H is the voltage from the Hall probes and d is the thickness of the sample or, equivalently, its size along the normal direction to the largest face). For sample 1a strong MR anisotropy is clearly seen in Fig. 3(a) with maximum values detected for $\mathbf{H} // [100]$ and it is accompanied by a dramatic decrease of the absolute values of ρ_H/H with the temperature lowering [Fig. 3(b)]. On the contrary, the reduced Hall resistivity ρ_H/H for $\mathbf{H} // [110]$ reveals only moderate changes with a negative minimum at the cage-glass transition temperature $T^* \sim 60$ K [44]. Thus, the values of ρ_H/H in crystal 1a differ by more than 3 times for these two directions of magnetic field. Simultaneously both the MR anisotropy and the strong temperature variation of the reduced Hall resistivity ρ_H/H for $\mathbf{H} // [100]$ depress essentially with the increase of residual resistivity ρ_0 in sample 2 [Figs. 3(c) and 3(d)]. This low temperature anisotropy becomes very small in sample 3 [Figs. 3(e) and 3(f)] with the highest ρ_0 value (shortest mean free path of the charge carriers). Taking into account that the Hall coefficient of normal uncompensated metal in strong magnetic fields is determined by the difference of electron and hole concentrations of $R_H = \rho_H/H \sim (n_e - n_h)^{-1}$ [58,59], it is extremely unusual to observe such a strong anisotropy of the reduced Hall resistivity ρ_H/H for the highest quality crystal (1a) in the LuB_{12} family (1–6).

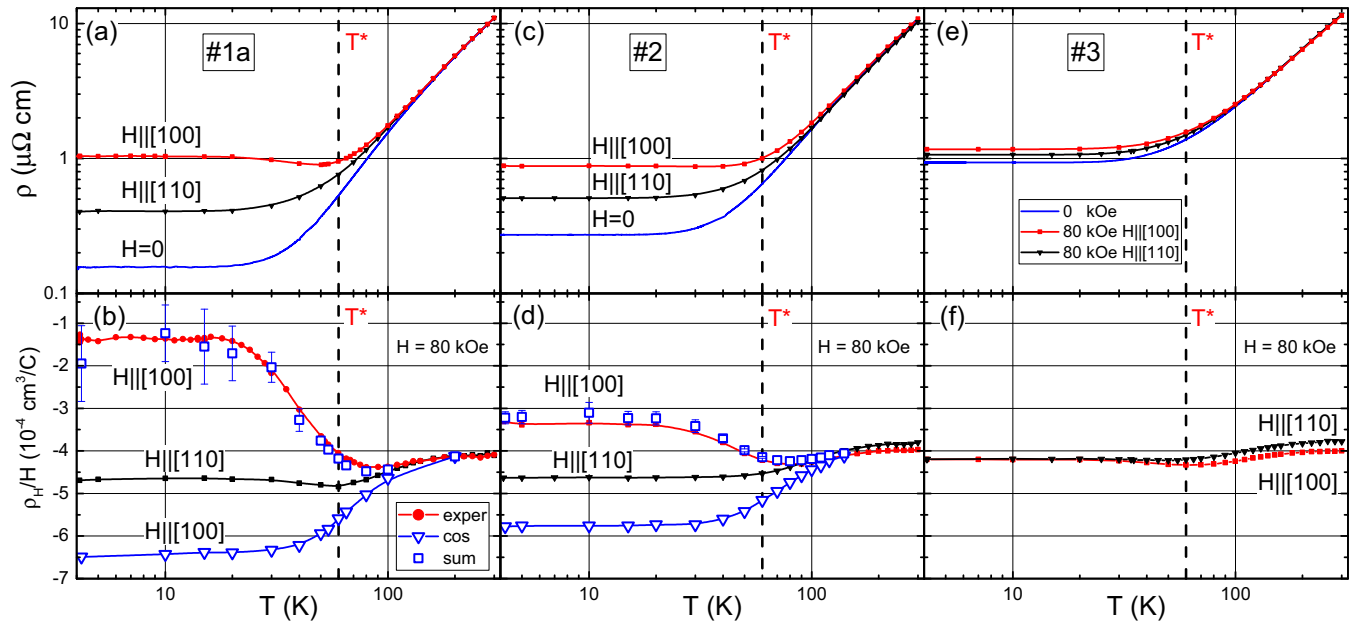


FIG. 3. Temperature dependencies of resistivity for the LuB_{12} crystals 1a (a), 2 (c), and 3 (e), and of the reduced Hall resistivity for crystals 1a (b), 2 (d), and 3 (f) at $H = 80$ kOe. Vertical dashed line marks the transition at $T^* \sim 60$ K to the cage-glass state. Large open symbols correspond to the ordinary Hall coefficient (marked as cos) and the sum of the ordinary and anomalous components (see text for details).

Figure 2(b) demonstrates the temperature dependencies of Hall mobility $\mu_H(T) = [\rho_H(T)/H]/\rho(T)$ estimated for crystals 1, 2, and 3 for two directions $\mathbf{H}//[100]$ and $\mathbf{H}//[110]$. It is worth noting that an unusually strong difference between $\mu_H(\mathbf{H}//[100])$ and $\mu_H(\mathbf{H}//[110])$ (about 6 times) appears for sample 1a just below $T^* \sim 60$ K in the disordered cage-glass phase of LuB_{12} . The ratio $\mu_H(\mathbf{H}//[100])/\mu_H(\mathbf{H}//[110])$ is reduced by a factor of 3 for sample 2 and becomes as low as 1.1 in the case of sample 3. The exponential behavior of Hall mobility $\mu_H(T) \sim T^{-\alpha}$ is observed in the temperature range 80–300 K for all LuB_{12} crystals; the $\alpha \approx 7/4$ exponent is detected for samples 1 and 2 with the large values of RRR = 40–70 and $\alpha \approx 3/2$ is estimated for sample 3 (RRR ~ 12) [Fig. 2(b)]. Note that the $\alpha = 3/2$ exponent is typical for the scattering of conduction electrons by acoustic phonons (deformation potential) and the increase of α values up to 7/4 in crystals 1 and 2 means that other scattering channels contribute mainly to the relaxation processes of charge carriers in the clean limit of LuB_{12} . The details of the phonon spectra of LuB_{12} have been detected in [38] allowing us to conclude in favor of the dominant carriers scattering on the quasilocal vibrations of the RE ions. So, relaxation processes due to scattering on both the boron optical phonons [38] in the presence of the JT distortions and the rattling modes of the RE ions [29–31] may be considered as dominant factors, which are responsible for the observed α increase in samples 1 and 2 of the RE dodecaboride with JT instability of the boron sublattice.

B. Magnetic field sweeping ($\mathbf{I}//[110]$)

The magnetic field dependencies of reduced Hall resistivity $\rho_H/H = f(H)$ [Fig. 4(a)], resistivity $\rho(H)$ [Fig. 4(b)], and Hall mobility $\mu_H(H)$ [Fig. 4(c)] show the results obtained for

sample 1a at $T = 4.2$ K (see also the Supplemental Material [37] for other LuB_{12} crystals). For $\mathbf{H}//[100]$ the amplitude of the reduced Hall resistivity demonstrates a dramatic (~ 10 times) decrease with the rise of magnetic field up to 140 kOe and, on the contrary, for $\mathbf{H}//[110]$ the amplitude of $\rho_H/H = f(H)$ increases only slightly. It is worth noting that the low-field values of ρ_H/H for $\mathbf{H}//[110]$ and $\mathbf{H}//[100]$ are just equal to each other [Fig. 4(a)], so any noticeable discrepancy is developed only above 10 kOe. Straightforward estimations of Hall mobility for the highest quality crystal 1a from the data of Figs. 4(a) and 4(b) result in high enough values of $\mu_H \sim 3000 \text{ cm}^2/(\text{V s})$ in low fields and small values of $\mu_H(H \approx 140 \text{ kOe}) \sim 18 \text{ cm}^2/(\text{V s})$ in high fields for $\mathbf{H}//[100]$ at liquid helium temperature. Note that the last values are about 40 times smaller than those detected for $\mathbf{H}//[110]$ [Fig. 4(c)]. This observation proves that the simple free electron model fails to extract any real microscopic parameters of charge carriers from the experimental data. Taking into account values of Fermi velocity $v_F \approx 1.1 \times 10^7 \text{ cm/s}$ [39] and the effective mass $m^* \sim 0.5m_0$ [42] a small enough average mean free path of charge carriers $l \sim 350 \text{ \AA}$ may be estimated even in the best quality single crystal 1 of LuB_{12} . It is worth noting also that the difference between estimated Hall mobilities for $\mathbf{H}//[100]$ and $\mathbf{H}//[110]$ decreases strongly for sample 2 with $\mu_H(H < 10 \text{ kOe}) \sim 1500 \text{ cm}^2/(\text{V s})$ and becomes much smaller for sample 3 where $\mu_H(H < 10 \text{ kOe}) \sim 420 \text{ cm}^2/(\text{V s})$ (see [37] for more detail) giving evidence for strong degradation of the mean free path in the 1-2-3 series.

C. Transverse MR anisotropy ($\mathbf{I}//[110]$)

The anisotropy of the transverse MR $\Delta\rho/\rho$ in LuB_{12} at liquid helium temperature is analyzed by discussing (i) the magnetic field dependencies of magnetoresistance collected

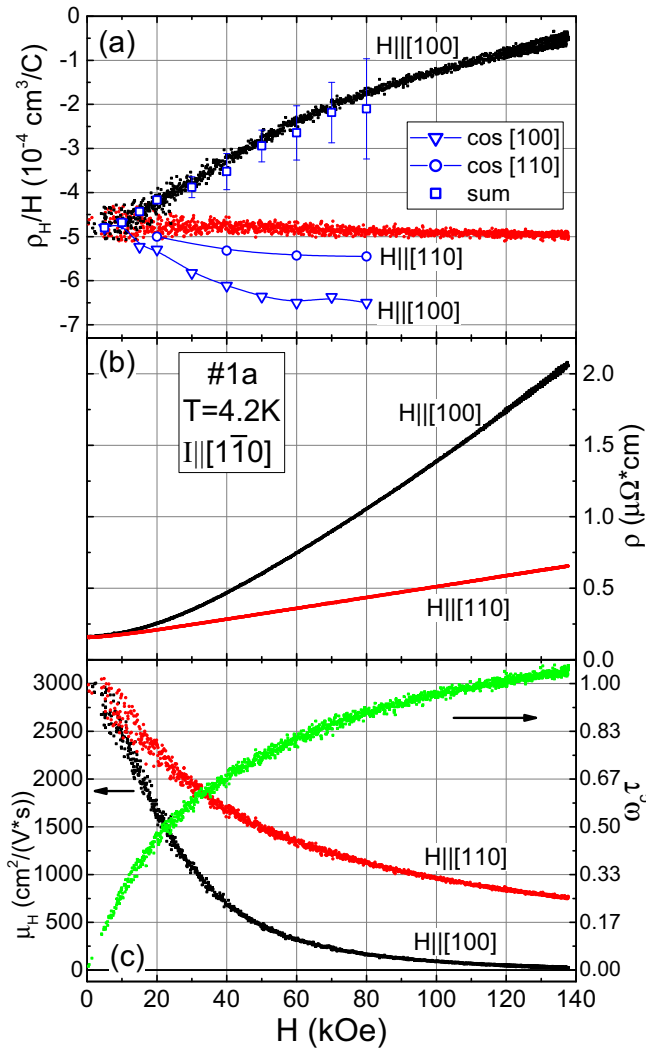


FIG. 4. Magnetic field dependencies of the reduced Hall resistivity (a), resistivity (b), and the Hall mobility (c) of the LuB_{12} crystal 1a at the liquid helium temperature. Large open symbols on (a) correspond to the ordinary Hall coefficient (marked as cos) and the sum of the ordinary and anomalous components (see text for details).

at different fixed angles φ between the normal \mathbf{n} to the (100) surface and the applied magnetic field [$\angle\varphi = (n^{\wedge}H)$, see the inset of Fig. 5(a)] and (ii) the angular dependence of magnetoresistance measured in various magnetic fields up to 80 kOe. The data of field and angle sweeping measurements for sample 1a are shown in Figs. 5(a) and 5(b), respectively. For comparison, Fig. 5(c) shows the anisotropy of MR detected for several LuB_{12} crystals having different RRR values (from 12 to 70) and the liquid helium Hall mobility ranging as 420–3000 $\text{cm}^2/(\text{V s})$ (see Fig. 4 and the data in [37]). It is easy to see that a whole set of extrema with small enough values of MR is detected on the $\Delta\rho/\rho(\varphi)$ dependencies in the angle range $54^\circ < \varphi < 126^\circ$ in the vicinity of the diagonals $\mathbf{H}//[110]$ and $\mathbf{H}//[111]$. At the same time, $\Delta\rho/\rho$ strongly increases within a wide range of angles ($-25^\circ < \varphi < +25^\circ$) when approaching $\mathbf{H}//[001]$ [Figs. 5(b) and 5(c)]. Note that the observed anisotropy of transverse magnetoresistance $\Delta\rho/\rho(\varphi)$ is very similar to the one reported earlier for the

LuB_{12} crystal at 0.5 K in 12 T [42]. This distorted cross-type anisotropy of MR is mostly pronounced in the polar plot shown in Fig. 6(a) and it could be evidenced either in favor of the existence of open trajectories on the Fermi surface [42], or it shows up in the presence of the filamentary structure of the dynamic charge stripes in LuB_{12} .

To shed more light on the details of the MR anisotropy in the nonmagnetic compound LuB_{12} the angular dependencies of $\Delta\rho/\rho(\varphi, T_0, H_0)$ have been studied for sample 1a in the strong magnetic field $H_0 = 80$ kOe in the wide temperature range 1.8–200 K. Figure 6(b) shows the 3D view of the transverse MR in the cylindrical plot. It is easy to see in Fig. 6(b) that the strongest increase of MR occurs when \mathbf{H} is oriented perpendicular to the filamentary structure of the quantum conduction channels ($\mathbf{H}//[001]$) while only moderate humps of MR are detected in the wide neighborhood of $\mathbf{H}//[110]$ dynamic charge stripe direction. Interestingly, both of the mentioned features are developed just below the cage-glass transition $T^* \sim 60$ K [marked by a dotted white line in Fig. 6(b)].

D. Angular dependencies of Hall resistivity ($\mathbf{I}//[110]$)

The selected angular dependencies of reduced Hall resistivity $\rho_H/H = f(\varphi, H_0)$ measured in various magnetic fields at liquid helium temperature are presented for two different orientations of the normal vectors $\mathbf{n}//[001]$ and $\mathbf{n}//[110]$ in Figs. 7 and 8, correspondingly (sample 1a, current axis $\mathbf{I}//[110]$; see also Fig. S2 in [37] for sample 2). The cosinelike behavior of Hall resistivity angular dependencies is natural for isotropic nonmagnetic metal reflecting the changes of the potential difference between two Hall probes due to varying transverse HE electric field [see the schema in the inset in Fig. 5(a)]. This simplified behavior is really observed for sample 3 [Figs. 7(c) and 8(c)] with smallest RRR, where Hall mobility is less than 450 $\text{cm}^2/(\text{V s})$ (Fig. S3 in [37]). On the contrary, an additional anomalous component contributes to the Hall signal for samples 1a and 2 in the configuration $\mathbf{I}//[1-10]$, $\mathbf{n}//[001]$ in the wide neighborhood of $\mathbf{H}//[001]$ direction (Fig. 7). The singularity is strongest for sample 1a with the largest RRR [$\mu_H(10 \text{ kOe}) \sim 3000 \text{ cm}^2/(\text{V s})$, Fig. 4(c)]. Indeed, the magnitude of the anomalous nonharmonic contribution for sample 1a at $H = 80$ kOe compensates substantially at the cosinelike component of the ordinary Hall effect near $\mathbf{H}//\mathbf{n}//[001]$, and the nonharmonic feature depresses for samples 2 and 3 (see Figs. 7(a)–7(c), and Fig. S6 in [37]). Moreover, the singularity is not observed when $\mathbf{H}//[110]$ for the same rotation axis ($\mathbf{I}//[1-10]$) and the other $\mathbf{n}//[110]$ configuration. Instead, two additional anomalous features of opposite sign have been detected on the $\rho_H/H = f(\varphi, H_0)$ data in the vicinity of $\mathbf{H}//[111]$ directions (see Fig. 8 for 1a).

The dramatic difference between ρ_H/H vs T (Fig. 3) and ρ_H/H vs H (Fig. 4) for $\mathbf{H}//[001]$ and $\mathbf{H}//[110]$ detected in our experiments and the qualitative dissimilarity of the $\rho_H/H = f(\varphi, H_0)$ data for $\mathbf{H}//[001]$ and $\mathbf{H}//[110]$ [shown by arrows in Figs. 7(a) and 8(a), respectively] make evident that the discovered singularity in the vicinity of $\mathbf{H}//[001]$ is responsible for very strong changes in the Hall signal observed in the $\mathbf{H}//[001]$ configuration. Indeed, the amplitude

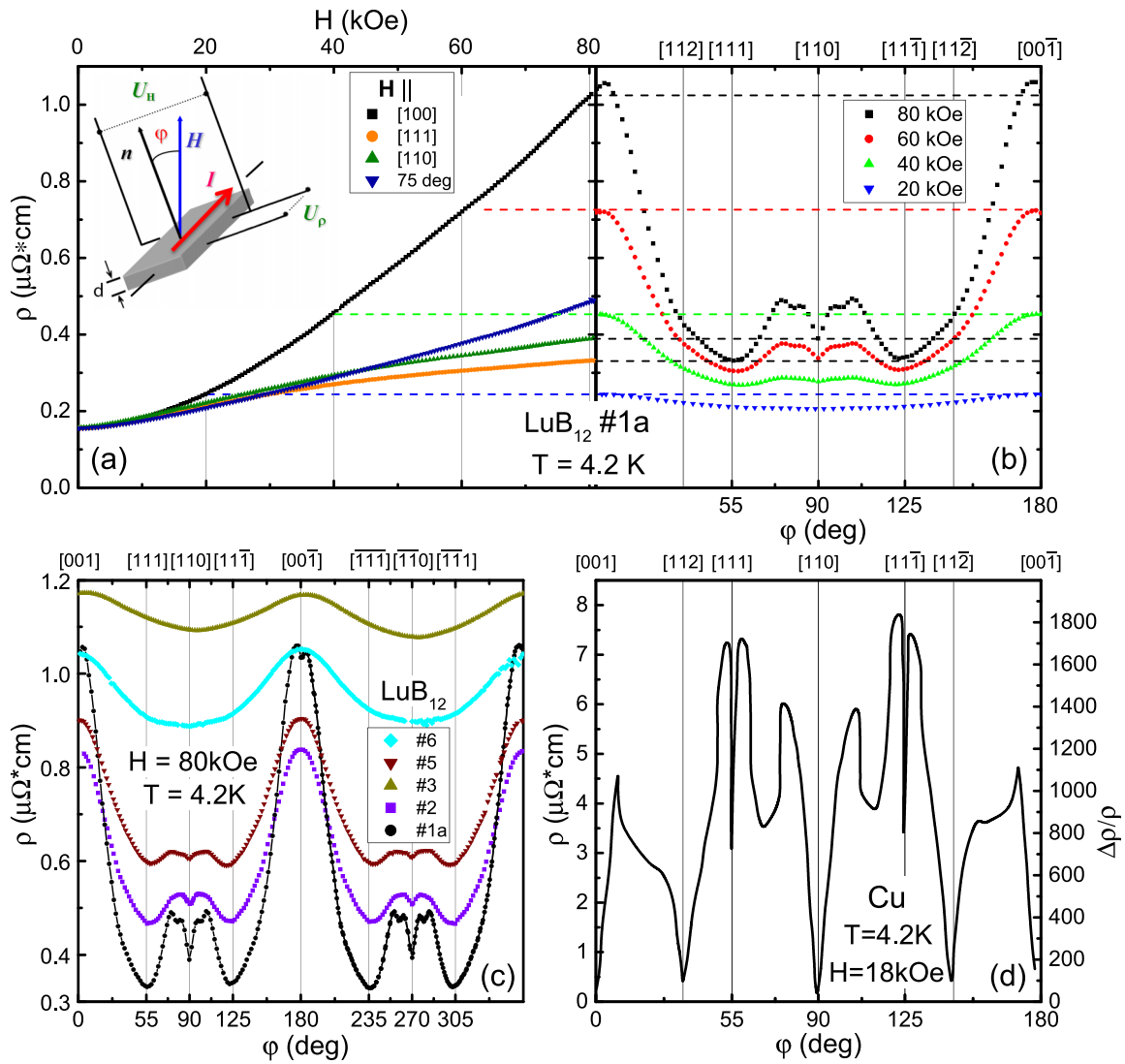


FIG. 5. Magnetic field (a) and angular (b) dependencies of resistivity of sample 1a of LuB_{12} at $T = 4.2\text{ K}$. For comparison the resistivity $\rho(\phi, T = 4.2\text{ K}, H = 80\text{ kOe})$ curves for several LuB_{12} samples are shown in (c). Schematic view of the sample for the galvanomagnetic measurements is presented in the inset in (a). (d) The results of similar transverse MR rotations for copper ($T = 4.2\text{ K}, H = 18\text{ kOe}$, RRR = 8000, adapted from [65]).

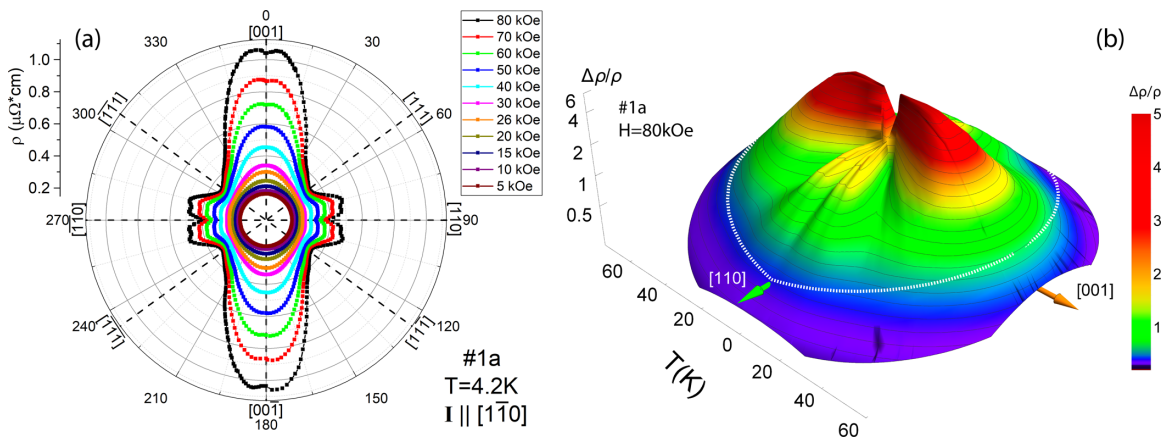


FIG. 6. (a) The polar plot of resistivity of sample 1a at $T = 4.2\text{ K}$. (b) The presentation in the cylindrical coordinates of the temperature dependence of MR of sample 1a at $H = 80\text{ kOe}$. Color shows the MR amplitude.

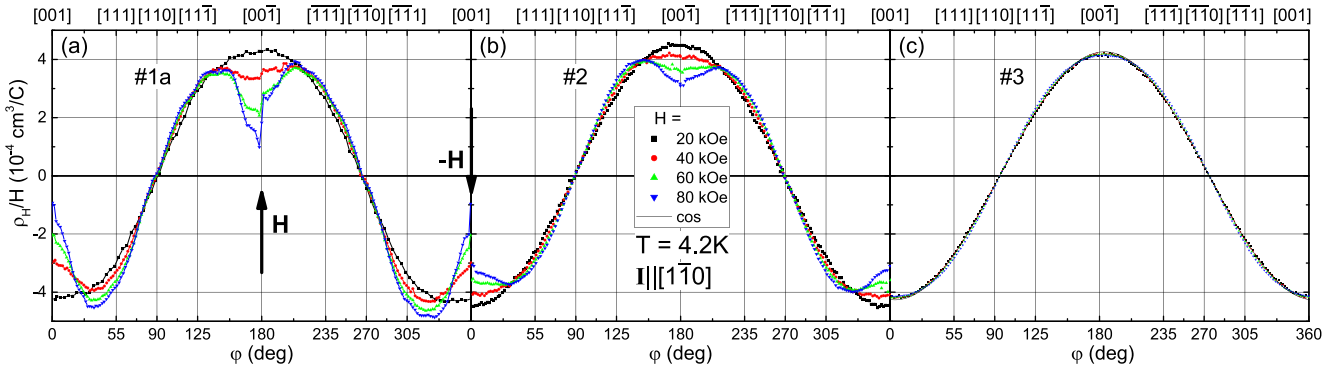


FIG. 7. Angular dependencies of the reduced Hall resistivity ρ_H/H for samples 1a (a), 2 (b), and 3 (c) at liquid helium temperature in the configuration $\mathbf{I}//[1-10]$, $\mathbf{n}//[001]$. Solid line in (c) demonstrates the cosin-type approximation. Vertical arrows in (a) show two H directions in the traditional, common-used technique of the Hall effect measurements.

of the feature detected near $\mathbf{H}//\langle 001 \rangle$ increases drastically both in magnetic field [see Figs. 7(a) and 9(b)] and with temperature decreasing below $T^* \sim 60$ K [see Fig. 9(a)]. It should be pointed out that the anomaly is observed in sample 1a (see also Fig. S7 in [37] for sample 2) when the external magnetic field $\mathbf{H}//\langle 001 \rangle$ is applied perpendicular to the $[110]$ direction of the dynamic charge stripes [see Fig. 1(a)]. This observation points to the possible relationship between the observed singularity and the effects of interaction of magnetic field with the filamentary structure of the quantum conduction channels. It is worth noting also that in low magnetic field ($H < 20$ kOe) the amplitude of the cosinlike contribution decreases essentially ($\sim 15\%$) in the sample sequence 1-2-3 (Fig. 7), so it should be suggested that the emergence of the infinite cluster of the dynamic charge stripes is accompanied by the moderate enhancement of the negative ordinary HE. More detailed quantitative analysis and general discussion of HE in LuB_{12} is presented below.

E. H - T variation of HE components ($\mathbf{I}//\langle 110 \rangle$)

To separate the ordinary and anomalous contributions to Hall effect the experimental data $\rho_H(\varphi, H_0, T_0)$ [Figs. 9(a), 9(b), and 10] were fitted by cosine law $\rho_{H0}(H_0, T_0)\cos\varphi$ in the segments $90^\circ \pm 20^\circ$ and $270^\circ \pm 20^\circ$ (see, e.g., Figs. 9(b)

and 10 for 1a and Fig. S7 in [37] for 2). The difference $\rho_H^{\text{an}}(\varphi, H_0, T_0) = \rho_H(\varphi, H_0, T_0) - \rho_{H0}(H_0, T_0)\cos\varphi$ was attributed to the additional specific component of HE. The temperature and field dependencies of the main term $R_H(T, H) \equiv \rho_{H0}/H$ (ordinary Hall effect, marked as “cos”) are shown in Figs. 3(b) and 4(a) for sample 1a, and in Figs. 3(d) and in [37] for sample 2. The H - T variation of the additional term $\rho_H^{\text{an}}/H(\varphi, H_0, T_0)$ for $\mathbf{n}//[001]$ configuration is presented in Figs. 9(c) and 9(d) for 1a and in Fig. S7 in [37] for 2. Figure 10 shows the reduced Hall resistivities ρ_H/H and $\rho_H^{\text{an}}/H = f(\varphi, H_0, T_0)$ detected in the $\mathbf{n}//[110]$ configuration of 1a at 4.2 K. It is clearly discerned from Figs. 9(c) and 9(d) that the largest ρ_H^{an}/H is observed for the $\mathbf{n}//[001]$ configuration around the $\langle 001 \rangle$ axis and the positive polarity of the additional specific component is opposite to the negative ordinary contribution in the Hall voltage of LuB_{12} . Besides, this anomalous term consists of two parts—smooth $\Delta_{\text{smooth}}(\varphi, H_0, T_0)$ and steplike $\Delta_{\text{step}}(\varphi, H_0, T_0)$ [see the legend in Figs. 9(c) and 9(d)]. The data analysis allows us to detect the changes in these Δ_{smooth} and Δ_{step} amplitudes both with the temperature variation [Fig. 9(e)] and magnetic field increasing [Fig. 9(f)]. Note that the sum of the specific component and ordinary Hall coefficient within the experimental accuracy is equal to Hall resistivity $\rho_H/H = f(\varphi, H_0, T_0)$ measured without sample rotation as a difference

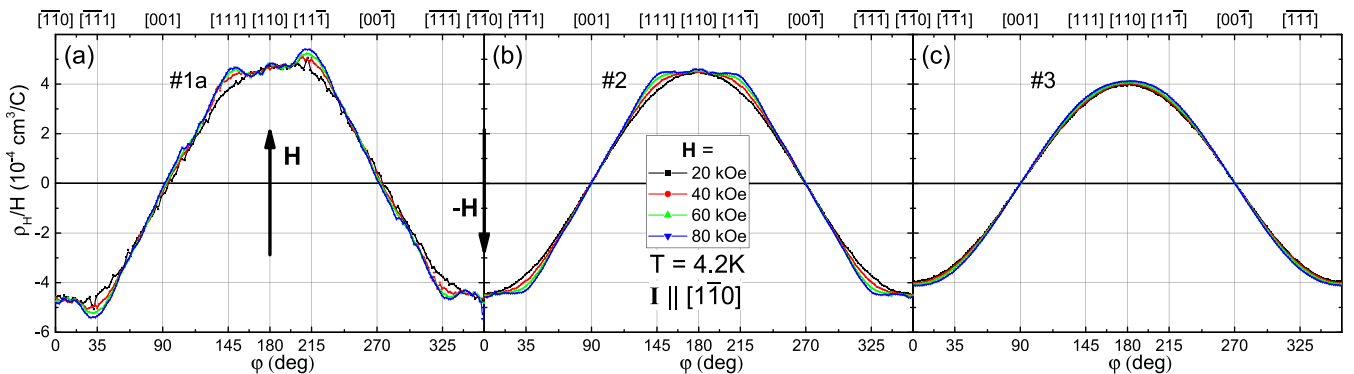


FIG. 8. Angular dependencies of the reduced Hall resistivity ρ_H/H for samples 1a (a), 2 (b), and 3 (c) at liquid helium temperature in the configuration $\mathbf{I}//[1-10]$, $\mathbf{n}//[110]$. Vertical arrows in (a) show two H directions in the traditional, common-used technique of the Hall effect measurements.

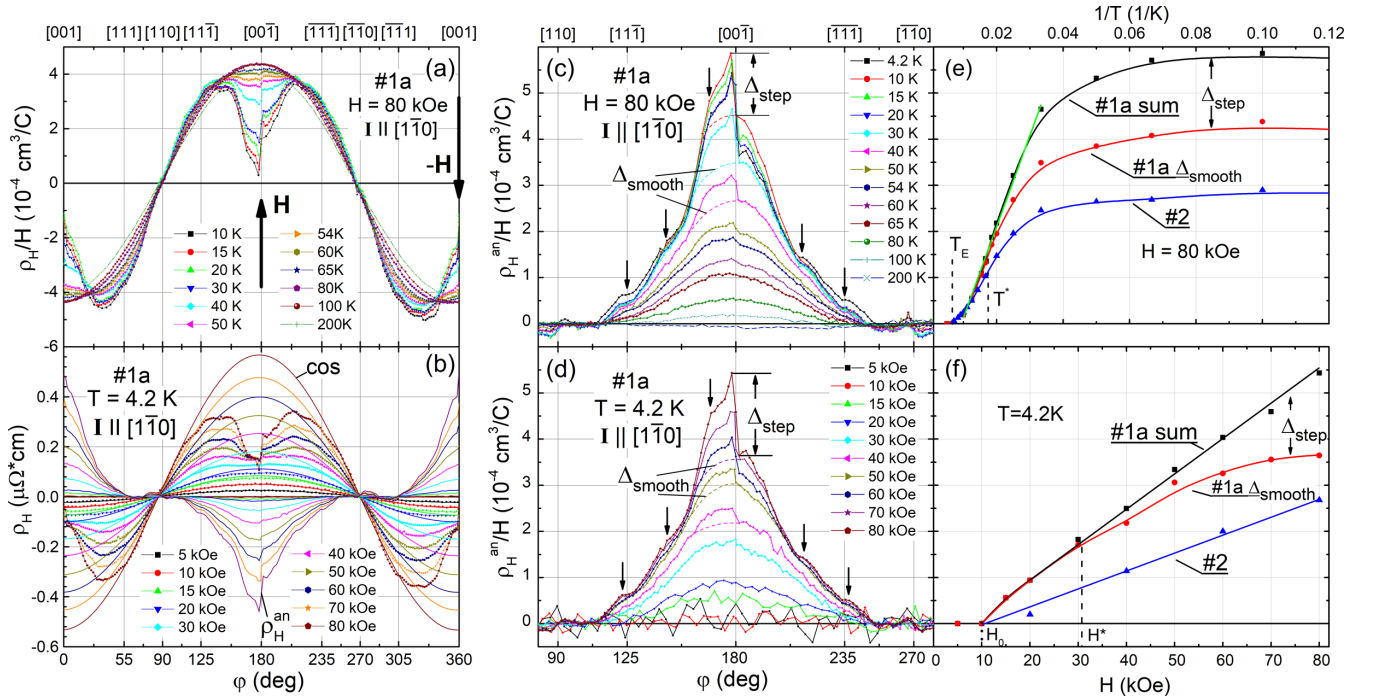


FIG. 9. Angular dependencies of the reduced Hall resistivities ρ_H/H and ρ_H^{an}/H in the configuration $\mathbf{I} // [110]$, $\mathbf{n} // [001]$ in sample 1a for various temperatures at $H = 80$ kOe (a) and (c) and in different magnetic fields at $T = 4.2$ K (b) and (d), correspondingly. Solid lines in (b) demonstrate the examples of the cosin-type approximation. Δ_{smooth} and Δ_{step} in (c) and (d) denote two anomalous components in the anomalous reduced Hall resistivity ρ_H^{an}/H . The reciprocal temperature plot in (e) shows the behavior of $\rho_H^{\text{an}}/H = f(T)$ detected in crystals 1a and 2. (f) The field dependence of $\rho_H^{\text{an}}/H = f(H, T = 4.2 \text{ K})$ and Δ_{smooth} , Δ_{step} components. T_E and T^* are the energy scales in the LuB_{12} (see text).

between the data for two opposite directions of magnetic field [see Figs. 3(a) and 4(a)], arguing in favor of the proposed explanation of the Hall voltage anomalies in the metal with dynamic charge stripes.

It is easy to see from Figs. 9(e) and 9(f) that the main specific component Δ_{smooth} appears in crystals 1 and 2 of

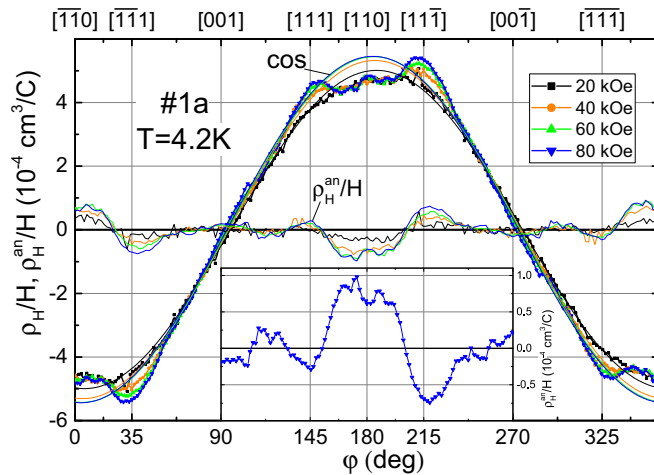


FIG. 10. Angular dependencies of the reduced Hall resistivities ρ_H/H and ρ_H^{an}/H in the configuration $\mathbf{I} // [1-10]$, $\mathbf{n} // [110]$ in sample 1a for various magnetic fields at $T = 4.2$ K. Solid lines demonstrate the examples of the cosin-type approximation. Inset shows a large scale view of $\rho_H^{\text{an}}/H = f(\varphi, H = 80 \text{ kOe}, T = 4.2 \text{ K})$.

LuB_{12} just below $T_E \sim 150$ K, where the development of the JT instability of B_{12} sublattice was found previously in various experiments. Indeed, it was shown in Raman studies [44] that temperature lowering leads to a sharp increase in the vibration density of states near T_E when the mean free path of phonons reaches the Ioffe-Regel limit and becomes comparable with their wavelength [60]. Moreover, the sharp peak of the relaxation rate in the vicinity of T_E is observed in μSR experiments with RB_{12} dodecaborides ($\text{R} = \text{Er}, \text{Yb}, \text{Lu}$) and $\text{Lu}_{1-x}\text{Yb}_x\text{B}_{12}$ solid solutions [61,62]. The authors [61,62] suggested that the large amplitude dynamic features in the μSR spectra are induced by the atomic motions within the B_{12} clusters.

Below $T^* \sim 60$ K in the cage-glass state of LuB_{12} [44] the steplike Δ_{step} component appears additionally to the Δ_{smooth} contribution [see Figs. 9(c) and 9(e)] and the amplitudes of these two terms increase simultaneously with the temperature lowering. At $T = 4.2$ K these anomalous positive components are not observed in low magnetic fields $H \leq 10$ kOe, and the only Δ_{smooth} contribution is detected on the angular dependencies $\rho_H^{\text{an}}/H(\varphi)$ in the range 10–30 kOe [Figs. 9(d) and 9(f)]. Then, the Δ_{step} feature appears above $H^* = 30$ kOe, and the $\Delta_{\text{step}}(H)$ and $\Delta_{\text{smooth}}(H)$ dependencies are found to be quite different. Indeed, the smooth component saturates in the fields up to 80 kOe, while the steplike one increases strongly resulting in a linear increase of the total amplitude [Fig. 9(f)]. When RRR decreases in the studied LuB_{12} crystals the additional Δ_{smooth} contribution is only observed with the linear field dependence [see curve for sample 2 in Fig. 9(f)].

The analysis of the temperature dependence $\rho_H^{\text{an}}/H = f(T, H_0 = 80 \text{ kOe})$ in crystals 1 and 2 allows us to reveal a hyperbolic type behavior $\rho_H^{\text{an}}/H = C^*(1/T - 1/T_0)$ [Fig. 9(e)]. The similar trend has been previously detected for an anomalous transverse even component of Hall voltage in strongly correlated electron systems (SCES) $\text{CeCu}_{6-x}\text{Au}_x$ [63] and $\text{Tm}_{1-x}\text{Yb}_x\text{B}_{12}$ [54]. Similar to the results for LuB_{12} [Fig. 9(e)] the anomalous hyperbolic component in $\text{Tm}_{1-x}\text{Yb}_x\text{B}_{12}$ appears in high enough magnetic fields at $T_E \sim 130\text{--}150 \text{ K}$, then increases drastically with the temperature lowering and saturates at liquid helium temperatures [54]. In the case of $\text{CeCu}_{6-x}\text{Au}_x$ [63] the transverse even effect is found to appear just below the structural phase transition at $T_s \sim 70 \text{ K}$ reaching maximum values in the quantum critical point $x_c = 0.1$. The findings were discussed in [54,63] in terms of anomalous Hall voltage caused by the interaction of external magnetic field with the filamentary structure of the many-body states. It is worth also noting that in the normal state of the HTSC, in addition to the crystalline anisotropy, the origin of the anomalous Hall signal is usually attributed to the appearance of stripes both on the surface and in the layers of the superconductors [18,64]. A similar data analysis has been developed here for the configuration ($\mathbf{I}//[1-10]$, $\mathbf{n}//[110]$) of sample 1a, and it was found that both the amplitude of the stripe-induced Hall effect (SIHE) and the ordinary (cosine-type) terms are much smaller in comparison with the case ($\mathbf{I}//[1-10]$, $\mathbf{n}//[001]$) [see Figs. 10 and 4(a)]. Moreover, the additional specific $\rho_H^{\text{an}}(\varphi)$ component in this configuration has several sign reversals with at least two intervals of negative values in the vicinity of the directions $\langle 111 \rangle$ (inset in Fig. 10).

Figure 11 demonstrates the decrease of both the additional Hall signal $\rho_H^{\text{an}}/H(T, H = 80 \text{ kOe})$ and the field induced resistivity component $\Delta\rho(T, 80 \text{ kOe}) = \rho(T, 80 \text{ kOe}) - \rho(T, 0 \text{ kOe})$ with the temperature increase [see Fig. 3(a)]. The behavior of these anomalous contributions may be well fitted by the analytical expressions $\rho_H^{\text{an}}/H = (\rho_H^{\text{an}}/H)_0 - AT^{-1}\exp(-T_0/T)$ and $\Delta\rho = \Delta\rho_0 - AT^{-1}\exp(-T_0/T)$ with the characteristic temperatures $T_0 = 114\text{--}140 \text{ K}$ for ρ_H^{an}/H and $140\text{--}150 \text{ K}$ for $\Delta\rho$ (the fits are shown by the solid lines in Fig. 11). Note that the behavior may be discussed in terms of the formation of the fragments (chains) of the dynamic charge stripes below $T_E \sim 150 \text{ K}$, and then the infinite cluster of the many-body states appears below $T^* \sim 60 \text{ K}$ in the cage-glass state [35].

F. HE and MR anisotropy for $\mathbf{I}//[100]$

In the previous part of the study we have focused only on the results of the charge transport measurements for the $\mathbf{I}//[110]$ configuration, and the data obtained under the sample rotation around the $\mathbf{I}//[110]$ current axis were discussed. Indeed, this configuration is the most important and useful for the analysis of the transverse ($\mathbf{I} \perp \mathbf{H}$) galvanomagnetic effects in LuB_{12} , because, from one side, the charge stripes are directed along $\langle 110 \rangle$ axes [30,31], and, from the other, all three principal directions $\mathbf{H}//[001]$, $[1-10]$, and $[1-11]$ are testified when rotating the crystal around this axis. At the same time, it is of extreme importance to investigate other $\mathbf{H}\text{-I}$ configurations and to characterize in more detail the charge transport

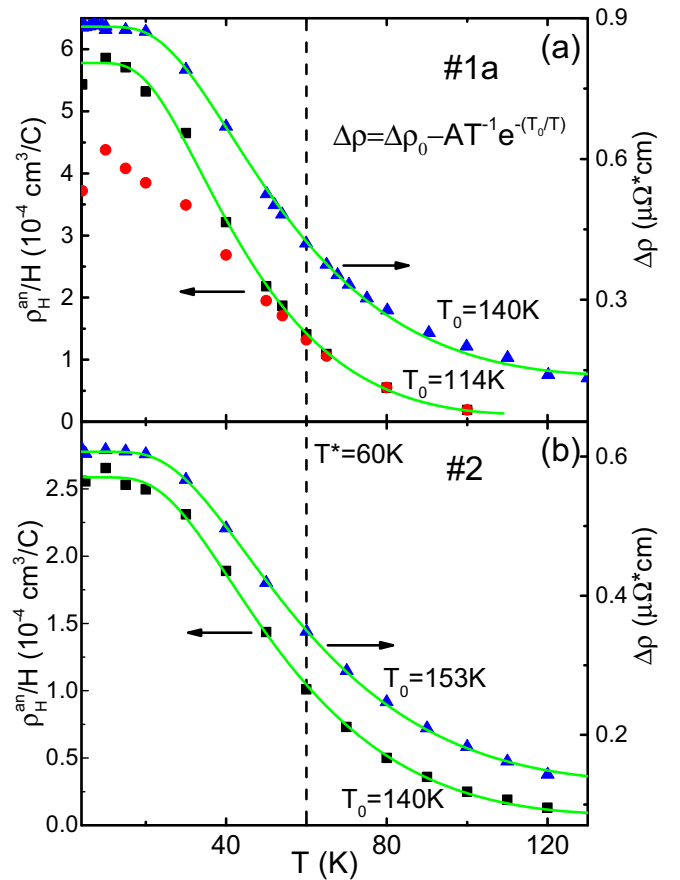


FIG. 11. The temperature dependencies of the anomalous reduced Hall resistivity ρ_H^{an}/H and resistivity $\Delta\rho$ components for samples 1a (a) and 2 (b). Solid lines show the analytical approximation by $(\rho_H^{\text{an}}/H, \Delta\rho) = (\rho_H^{\text{an}}/H, \Delta\rho)_0 - AT^{-1}\exp(-T_0/T)$. Vertical dashed line marks the transition at $T^* \sim 60 \text{ K}$ to the cage-glass state.

anisotropy induced by the filamentary structure of quantum conduction channels in this heterogeneous medium. To check it both the transverse MR and Hall resistivity have been studied here with the current direction $\mathbf{I}//[100]$. Figures 12(a) and 12(b) show the angular (at $T = 4.2 \text{ K}$) and temperature dependencies of resistivity, respectively, measured for sample 2 in strong magnetic field ($H = 80 \text{ kOe}$). It is clearly discerned from Figs. 12(a) and 12(b) that below $T^* \sim 60 \text{ K}$ the resistivity increases noticeably. Simultaneously, (i) two $\langle 110 \rangle$ directions in the (001) plane of the fcc LuB_{12} lattice became nonequivalent and (ii) the $\rho(\varphi)$ dependence demonstrates a set of minima and maxima separated by $\Delta\varphi \approx 22.5^\circ$. The polar plot presented in Figs. 12(c) and 12(d) shows the variation of the angular MR dependencies in magnetic field for samples 2 and 1c of LuB_{12} , correspondingly. Usual fourfold anisotropy of transverse MR is detected for sample 2 in the low magnetic fields $H \leq 40 \text{ kOe}$ when the current is applied along the cube edge in the fcc lattice [Fig. 12(c)]. In higher magnetic fields the symmetry lowers dramatically when two $\langle 110 \rangle$ face diagonals become quite different. On the contrary, the fourfold symmetry for the crystal 1c is found to break already for $H \geq 20 \text{ kOe}$ [Fig. 12(d)], so that two cubic edges $[100]$ and

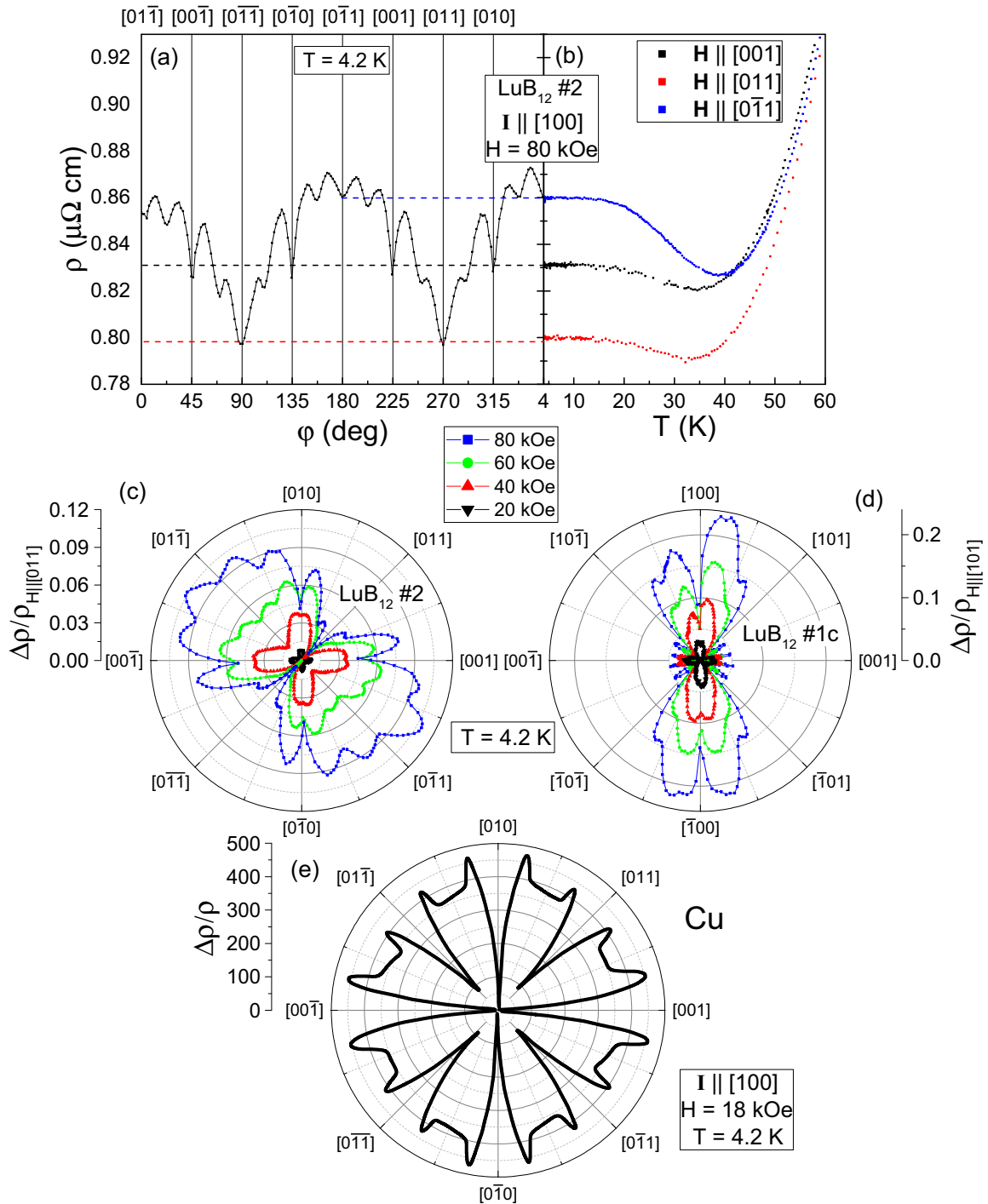


FIG. 12. (a) Angular ($T = 4.2$ K) and (b) temperature dependencies of resistivity of sample 2 of LuB₁₂ at $H = 80$ kOe. For comparison, the polar plots (c) and (d) at $T = 4.2$ K demonstrate the angular dependencies of the normalized MR for samples 2 and 1c, correspondingly. (e) The results of similar transverse MR rotations for copper ($T = 4.2$ K, $H = 18$ kOe, RRR = 8000, adapted from [81]).

[001] happen to be nonequivalent. It is seen from Fig. 13(a) that the dramatic symmetry breaking is developed in sample 1c in the cage-glass state of LuB₁₂ (below $T^* \sim 60$ K), so that 16 equidistant directions of magnetic field corresponding to the local maxima of transverse MR are detected in the sample.

It is also worth noting that two [010]- and [001]-elongated bars of LuB₁₂ with equivalent (100), (010), and (001) faces

were cut from one ingot in our previous study [29] [see, e.g., samples 1b and 1c in the inset of Fig. 14(a)]. At liquid helium temperatures their MR were found to be strongly anisotropic, demonstrating similar resistivity oscillations with the well-defined maxima separated by the period of $\Delta\phi \approx 22.5^\circ$ [Figs. 12(a) and 13(a)]. We have also compared two sets of Hall effect data for cognate crystals 1b and 1c (Fig. 14) where the z axis is the same for both samples and the magnetic

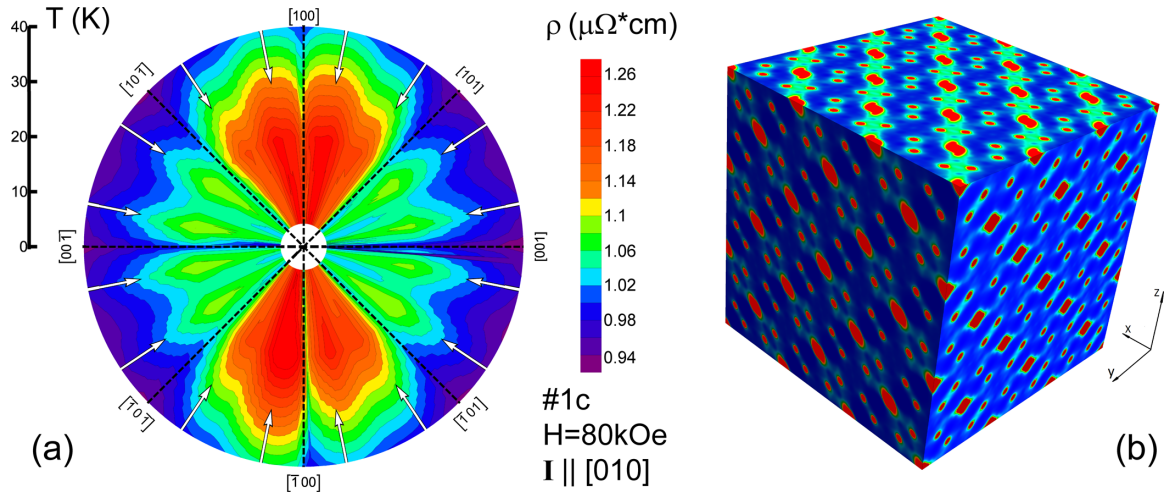


FIG. 13. (a) The presentation in the polar coordinates of the temperature dependence of resistivity of sample 1c at $H = 80$ kOe ($\mathbf{I} // [010]$). Color shows the resistivity amplitude, and arrows mark the harmonics (see text). (b) The map of the electron density distribution in LuB_{12} obtained by the maximum entropy method [30,31].

field is applied transverse to the stripes ($\mathbf{H} // \mathbf{n} // [001]$). As a result, the reduced Hall resistivity in both crystals demonstrates similar anomalies in the wide neighborhood of the $\langle 001 \rangle$ direction. Note also that angular oscillations are also observed on the reduced Hall resistivity in addition to the main feature in the $\rho_{\text{H}}^{\text{an}}/H = f(\varphi, H = 80 \text{ kOe})$ curve, they being the most noticeable for sample 1c [see the $\rho_{\text{H}}^{\text{an}}/H$ data in Fig. 14(b)].

IV. DISCUSSION

A. Fermi surface (FS) effects

At low temperatures the scattering of charge carriers in pure metals is sensitive to the topology of the Fermi surface (FS). Both quantum oscillations [de Haas–van Alphen

(dHvA)/Shubnikov–de Haas (SdH) effects] and specific anomalies on the angular dependencies of magnetoresistance and Hall resistivity are observed in the metals with open and closed electron orbits in high magnetic fields if $\omega_c \tau \gg 1$ (ω_c is the cyclotron frequency and τ is relaxation time) [59,65,66,81]. In LuB_{12} the dHvA signal has been measured at 0.35 K for all field directions within the (010) and (011) planes in the field range 9–12 T [42], but SdH oscillations at the same temperature have been found only for one combination of $\mathbf{I} // [110]$ and $\mathbf{H} // [001]$ [42]. In our measurements at $T = 4.2$ K weak quantum oscillations have been also detected in magnetoresistance and Hall resistivity above 10 T under the same conditions ($\mathbf{I} // [110]$ and $\mathbf{H} // [001]$, see [37] for more detail). Note that both dHvA [67] and SdH oscillations depress totally when temperature increases over 10 K. So, even if the rough estimation of $\omega_c \tau (\approx \mu_{\text{H}} H)$ in

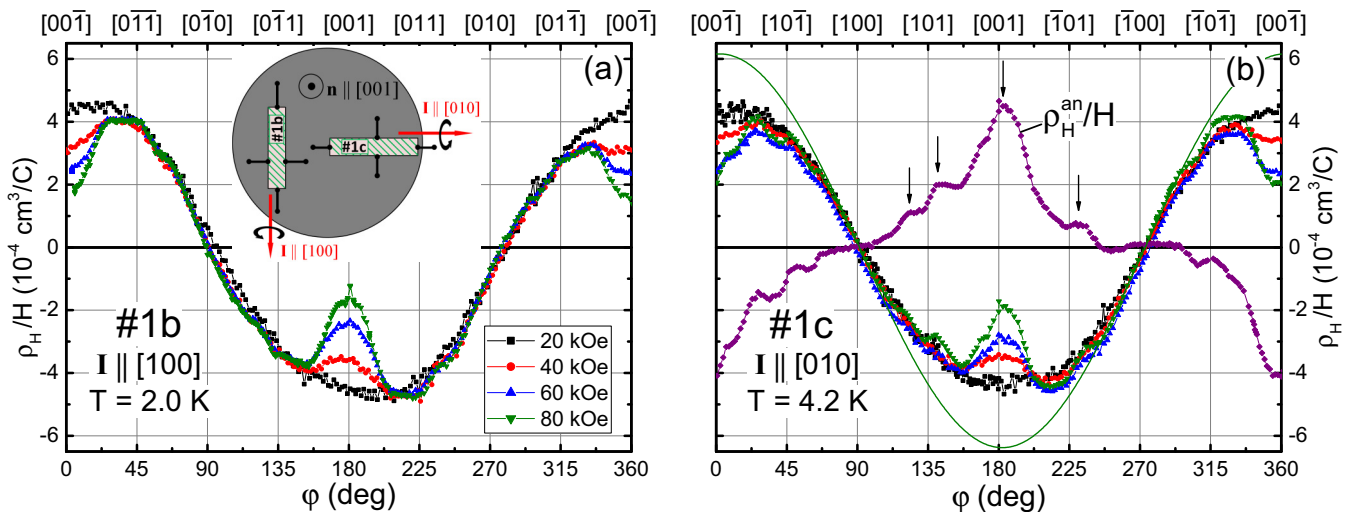


FIG. 14. Angular dependencies of the reduced Hall resistivity ρ_{H}/H for samples 1b (a), ($\mathbf{I} // [100]$) and 1c (b) ($\mathbf{I} // [010]$) at liquid helium temperature in the configuration $\mathbf{n} // [001]$. Solid line in (b) demonstrates the cosine-type approximation, and $\rho_{\text{H}}^{\text{an}}/H(\varphi)$ shows the anomalous component. Arrows mark the harmonics (see text). Inset shows schematically how samples 1b and 1c are cut from the single crystalline disk of LuB_{12} .

the purest crystals of LuB₁₂ results in $\omega_c\tau < 1$ in magnetic fields below 12 T [see data for sample 1 in Fig. 4(c)], the anisotropy of the electron transport which could be induced by FS topology should be properly treated. Besides, the straightforward estimation of the concentration of conduction electron from high-temperature Hall constant $R_{H0} \approx -4 \times 10^{-4} \text{ cm}^3/\text{C}$ (Fig. 3) results in $n_0 \approx 1.56 \times 10^{22} \text{ cm}^{-3}$. The value in this metal with one conduction electron per formula unit [40–43] is considerably higher than the concentration of Lu ions ($n_{\text{Lu}} = 4/a^3 \approx 0.96 \times 10^{22} \text{ cm}^{-3}$, $a \approx 0.746 \text{ nm}$ is the lattice parameter [29–31,68]). This means that at least two groups of charge carriers (electrons and holes) with different effective concentrations and mobilities contribute effectively to charge transport in this nonmagnetic metal at room and low temperatures.

This suggestion is supported by the FS structure of LuB₁₂ that consists of one hole and two electron sheets [42,43,67,69]. This “monster” in the LuB₁₂ lower conduction band [70] (see also [37]) is very similar to that of the noble metals (Cu, Au, and Ag) if we allow for the hole-electron asymmetry of the related FS sheets [42]. Indeed, similar to copper the holelike *open orbits* in LuB₁₂ are located close to $\langle 001 \rangle$, $\langle 110 \rangle$, and $\langle 111 \rangle$ [59,65,66,71,72] while the nearest vicinity of all these axes provides only the *closed FS sections* for $\mathbf{H} // \langle 001 \rangle$, $\mathbf{H} // \langle 110 \rangle$, and $\mathbf{H} // \langle 111 \rangle$ (see [59,65,71] for more details). This feature results in the anisotropic MR behavior with twin peak structure around $\mathbf{H} // [001]$ and $\mathbf{H} // [110]$ and the saturation of $\rho/\rho_0 \approx 4$ for $\mathbf{H} // [111]$, which was detected in LuB₁₂ at $T = 0.5 \text{ K}$ and $\mu_0 H = 12 \text{ T}$ [42] [see also Figs. 5(b) and 5(c)] and was explained assuming several bunches of open orbits in the lower conduction band of this metal [42].

The similar topology of FSs in LuB₁₂ and Cu provides us the explanation for the origin of the resistivity oscillations detected on the $\rho(\varphi)$ dependencies for $\mathbf{I} // [010]$ [Figs. 12(a) and 13(a)]. Indeed, the similar structure of the resistivity anomalies associated with the open orbits contribution was earlier detected for copper [65] [see polar plot Fig. 12(e)]. Note that the amplitude of these angular anomalies in the magnetoresistance of copper, to be about 100–500 [Fig. 12(e)], exceeds drastically the one in LuB₁₂ [~ 0.02 – 0.1 , Figs. 12(a)–12(d)] due to the higher quality of the Cu single crystals. Nevertheless, the similar positions of these resistivity maxima and the increase of their relative amplitude when increasing magnetic field or/and lowering of temperature [Figs 12(c), 12(d), and 13(a)] allow us to attribute these features to the contribution of open orbits, which appear for the particular directions of applied magnetic fields. In this approach the peak features in magnetoresistance have to be accompanied by the minima in the Hall resistivity [59], which are transformed in the maxima under our subtraction procedure and can be clearly resolved in the angular dependencies of the anomalous contribution $\rho_{\text{H}}^{\text{an}}/H$ [see arrows in Fig. 14(b)].

At the same time we have to note the principal dissimilarity in the MR behavior for copper and lutetium dodecaboride. In high quality crystals of copper the FS topology results in the MR saturation for all the principal directions of applied magnetic field [see deep minima in Fig. 5(d)], the unsaturated MR growth due to open orbits being detected close to all these axes. In LuB₁₂ the trend to $\rho(H)$ saturation is observed

for $\mathbf{H} // [110]$ and $\mathbf{H} // [111]$ only while MR does not saturate in the wide vicinity of $\mathbf{H} // [001]$ (see Figs. 4(b), 5(a) and 5(b) and [42]). Note also that the strongest MR increase in Cu is observed when $\mathbf{I} // [110]$ and the magnetic field is applied along the necks of the monster ($\mathbf{H} // [111]$) [37,70]. Moreover, the MR anomaly at $\mathbf{H} // [001]$ appears in LuB₁₂ at high temperatures (below $T_E \sim 150 \text{ K}$, see Fig. 11) even for the crystals with smaller mobilities (Fig. 5(c) and [37]). Finally, the position and the width of the MR anomaly in LuB₁₂ at $\mathbf{H} // [001]$ are just identical to those of the extra specific contribution to Hall effect, which was extracted as $\rho_{\text{H}}^{\text{an}}/H$ in our study (see Secs. III E and III F and Fig. 11).

In searching for the mechanism responsible for the appearance of the anomaly in MR and HE at $\mathbf{H} // [001]$ note that the SdH quantum oscillations (see Fig. 4 and [36]) were measured for $\mathbf{H} // [001]$ at liquid helium temperatures in magnetic field $\mu_0 H > 10 \text{ T}$ in this metal with small enough average mobility of charge carriers [see $\omega_c\tau$ for sample 1 in Fig. 4(c)]. This means that there is at least one group of carriers, for which the high-field limit $\omega_c\tau \gg 1$ is valid. According to [42], the quantum SdH oscillations for $\mathbf{H} // [001]$ are contributed from the holelike orbits in the lower conduction band of LuB₁₂. This R_{100} orbit (“four cornered rosette” [70]) corresponds to the particular dHvA α_2 branch with the extreme area $S_{\alpha_2} \approx 25 \text{ nm}^{-2}$ [42]. If we suggest that these holelike regions are deformed spheroids in the W points of the Brillouin zone [42] one can estimate the effective parameters of these charge carriers. In particular, leaving the geometrical factor $G = V_{\alpha_2}/S_{\alpha_2}^{3/2} = 0.9$ (V_{α_2} and S_{α_2} the volume and the extreme area of the FS sheet) to be intermediate between $G = 1$ for cuboid and $G = 4/(3\pi^{1/2}) \approx 0.75$ for spheroid, the volume of the FS sheet can be estimated as $V_{\alpha_2} = 0.9S_{\alpha_2}^{3/2} \approx 113 \text{ nm}^{-3}$, which corresponds to the $n_{\alpha_2} \approx 2.7 \times 10^{21} \text{ cm}^{-3}$ and the effective Hall constant $R_{\text{H}}^{\alpha_2} = (|e|n_{\alpha_2})^{-1} \approx +2.3 \times 10^{-3} \text{ cm}^3/\text{C}$. The condition $R_{\text{H}}^{\alpha_2}(\sigma_{\alpha_2})^2 \sim R_{\text{H}0}(\sigma_0)^2$ results in the conductivity ratio $\sigma_{\alpha_2}/\sigma_0 \approx 0.42$ (σ_{α_2} and σ_0 are the hole conductivity and the average conductivity, respectively). The corresponding mobility ratio is estimated as $\mu_{\alpha_2}/\mu^* = (\sigma_{\alpha_2}n_0)/(\sigma_0n_{\alpha_2}) \approx 2.4$ resulting in the value of $\mu_{\alpha_2} \approx 7100 \text{ cm}^2 \text{ V}^{-1} \text{ s}^{-1}$. Thus, for these holelike orbits the high-field limit $\omega_c\tau \sim \mu_{\alpha_2}H_0 \sim 2\pi$ gives the reasonable value of $\mu_0 H_0 \sim 9 \text{ T}$ that agrees very well with the onset of SdH oscillations on the $\rho(H)$ and $\rho_{\text{H}}(H)$ data for $\mathbf{H} // [001]$ (Fig. 4 and [37]). The estimation of relaxation time results in the value of $\tau = \mu_{\alpha_2}m_{\alpha_2}^*/|e| \approx 2 \text{ ps}$ if we allow for the effective mass value $m_{\alpha_2}^* \approx 0.53 m_0$ [42]. The corresponding Dingle temperature $T_D \approx 0.6 \text{ K}$ and the high enough value of related parameter $\mu_0 H \tau \approx 16 \text{ T ps}$ [67] prove these quantum oscillations to be observable at liquid helium temperatures.

The above speculations allow us to suggest that the wide anomaly detected at $\mathbf{H} // [001]$ in the angular dependencies of MR and Hall resistivity may be induced by a strong relaxation time anisotropy rather than by any specific contribution of the open orbits on the LuB₁₂ FS, which seem to produce only narrow anomalies on the MR data in available magnetic fields (see Fig. 5(b) and 5(c) and [42]). The anisotropy of scattering time is more pronounced in Hall effect data where noticeable deviations from cosine behavior are well resolved below 150 K [Figs. 9(c) and 9(e)]. It should be noted here that these

temperatures are comparable to the vibrational energies of the rare earth ions (scaled by Einstein temperature $T_E \approx 150$ K) so a strong electron-phonon interaction has to smear out any FS induced features. In this respect, any consistent model allowing for scattering time anisotropy should comprise the microscopic mechanisms, which are responsible for the formation of these “hot” and “cold” regions of FS, and the related factors, which prevent any effective mixing of these different electron states.

B. Stripe induced Hall effect (SIHE)

The above consideration shows that any model based exclusively on the particular FS topology is insufficient to explain not only the origin of the MR anomaly for $\mathbf{H}//[001]$ and $\mathbf{I}//[1-10]$ [Figs. 5(b), 5(c), and 6(b)], but also the extremely narrow steplike feature Δ_{step} and a wide range Δ_{smooth} component detected in the angular dependencies of Hall resistivity at $\mathbf{H}//[001]$ for all directions of applied current [Figs. 7, 9, and 14(b)]. Indeed, the wide MR anomaly at $\mathbf{H}//[001]$ is observed even for the crystals of LuB_{12} with a small enough mobility (Fig. 5(c) and [37]) and at high temperatures up to 150 K (Fig. 11). It should be pointed out that the steplike feature in Hall resistivity at $\mathbf{H}//[001]$ is detected only for one particular combination of $\mathbf{H}//[001]$ and $\mathbf{I}//[110]$ in the highest quality crystals of LuB_{12} at temperatures up to $T^* \sim 60$ K [see Fig. 9(c)]. In this respect we note that the effects of symmetry lowering were previously established in the MR study of LuB_{12} (Figs. 12 and 13) as the unique features of the RE dodecaboride with the dynamic charge stripes. Indeed, the corresponding electron density (ED) distribution in the LuB_{12} crystals, which was deduced from the analysis of the x-ray diffraction data with the help of the maximal entropy method (MEM) [30], is strongly inhomogeneous [Fig. 13(b)]. Assuming that pinning of the dynamic charge stripes on the randomly arranged defects and impurities fixes the selected direction in the dodecaboride matrix [Fig. 13(b)], it is natural to associate the fcc symmetry breaking with the nanoscale phase separation effects and emerging filamentary structure of conduction channels in the LuB_{12} matrix.

Note here that the discussed anomalies found in the angular dependencies of magnetoresistance and Hall resistivity are specific for both magnetic and nonmagnetic $\text{Ho}_x\text{Lu}_{1-x}\text{B}_{12}$ compounds [73–80]. These common features increase strongly below $T^* \sim 60$ K (see Fig. 11) in the cage-glass state [35,44]. In our opinion, these similarities favor the explanation for the significant MR increase in the vicinity of $\mathbf{H}//[001]$, which has been proposed recently in [35,73,75]. We consider the strong interaction of the dynamic stripes along the [110] direction with the transverse external magnetic field [Fig. 1(a)] as the possible reason for the detected increase of the amplitude of the negative cosine-type component (absolute values of the ordinary Hall effect), which is clearly observed with an increase of external magnetic field [Fig. 4(a)]. This behavior (see Figs. 7 and 8 and Figs. S4 and S5 in [37]) is accompanied by the changes of the average mobility in the LuB_{12} crystals. The measurements of optical conductivity in LuB_{12} [39] revealed that the conduction band consists of (i) Drude electrons and (ii) nonequilibrium (hot) charge carriers involved in the collective modes and

seen in the conductivity spectra as overdamped oscillators. As nonequilibrium electrons amount to about $\sim 70\%$ of the total electron concentration, the related approach should include some redistribution of electrons between these two electron subsystems. A rough estimation obtained from the optical conductivity spectra [69] proves that the relative number of the Drude-type and hot charge carriers does not change in LuB_{12} at low temperatures. We suggest that strong impurity scattering provokes fast thermalization of the hot electrons, but, on the contrary, strong external magnetic field increases the number of electrons in these dynamic charge stripes. As a result, both the impurity concentration and external magnetic field may be considered as two factors, which are responsible for the redistribution of charge carriers between the nonequilibrium and Drude-type electron subsystems in the heterogeneous medium of LuB_{12} nonmagnetic metal with dynamic charge stripes.

This redistribution may also increase the amplitude of the Hall effect component, which is induced by the stripes (SIHE). In this scenario the low temperature enhancement of the negative ordinary Hall coefficient [marked as \cos in Fig. 4(a)] observed in a strong magnetic field should be attributed to the decrease of free electron concentration n_e . The n_e evolution is accompanied by a dramatic increase of the SIHE amplitude [Figs. 9(d), 9(f), 11, and 14]. In this picture the field-induced decrease of a number of carriers $\Delta n_e/n_e$ in the LuB_{12} matrix is dependent on the direction of external magnetic field. The effect happens to reach the largest value ($\sim 30\%$) for \mathbf{H} to be transverse to dynamic charge stripes ($\mathbf{H}//\mathbf{n}//[001]$, see schema in Fig. 1(a)), while only relatively small ($\sim 10\%$) changes are observed for $\mathbf{H}//[110]$ [Fig. 4(a)]. The validity of the SIHE scenario could be verified in the future both by precise magnetotransport studies and optical measurements in high magnetic field. Note here only that the redistribution in magnetic field of the charge carriers between the Drude-type and hot, nonequilibrium electron subsystems may be attributed to the reasons of emergence of anomalous Hall effect and MR in the dodecaborides with magnetic RE ions, e.g., such as $\text{Ho}_x\text{Lu}_{1-x}\text{B}_{12}$ [73–80].

V. CONCLUSION

Summarizing the specific features of magnetoresistance and Hall resistivity found in the present study for the nonmagnetic metal LuB_{12} with dynamic electron stripes, we outline the different factors, which may result in the anomalies of electron transport in this material. While some peculiarities found in the angular dependencies of MR (16 maxima for $\mathbf{I}//[100]$ and twin peak fine structure around $\mathbf{H}//[001]$ and $\mathbf{H}//[1-10]$ for $\mathbf{I}//[110]$) and Hall resistivity may be definitely associated with the presence of open orbits in the corresponding sections of FS, the origin of the wide feature at $\mathbf{H}//[001]$ found both in MR and HE requires further theoretical consideration. The estimations based on the FS topology show that this anomaly could appear due to the relevant contribution of the holes with large enough mobility ($7100 \text{ cm}^2 \text{ V}^{-1} \text{ s}^{-1}$) and relaxation time (2 ps), but these parameters decrease dramatically at high temperatures (up to 150 K) prohibiting this kind of scenario. In contrary, the inhomogeneous distribution of electron density (nanoscale phase separation) in LuB_{12}

initiated by the cooperative JT effect in the B_{12} clusters in the presence of the rattling modes of Lu ions may also result in the additional component in Hall resistivity. In the last case the configuration dependent contribution to Hall effect arises due to interaction of magnetic field with the filamentary structure of dynamic charge stripes, which pin occasionally along one of $\langle 110 \rangle$ principal directions of the fcc lattice. We suggest that the charge transport symmetry breaking is caused by the field-stripes interaction developed in LuB_{12} in a strong magnetic field. However, the approach requires a careful consideration of the processes, which determine the redistribution of the charge carriers between “cold” (Drude-like) and “hot” (nonequilibrium) channels. Indeed, the strong anisotropy of relaxation time with its low enough average value may be induced by the cooperative JT instability of the B_{12} clusters in LuB_{12} . The related ferrodistorptive effect in the rigid boron cage induces the periodic changes in the $5d-2p$ hybridization modulating the width of the conduction band and increasing the intensity of charge carrier scattering. In this scenario the

related “breathing” of FS should lead to periodic changes of size for both the belly and necks of the holelike FS monster [37] and may be considered as the main factor responsible for the average τ decrease and the depression of the SdH oscillations in LuB_{12} . In this respect the steplike anomaly in Hall resistivity detected only for one combination of $\mathbf{H}_i/[001]$ and $\mathbf{I}_i/[110]$ in the high quality single crystals of LuB_{12} (see Secs. III E and III F) may be treated as a key feature to check the validity of the theoretical approaches proposed for explanation of the magnetotransport anomalies in this compound.

ACKNOWLEDGMENTS

This work was supported by the Russian Science Foundation, projects No. 17-12-01426 and No. 21-12-00186 (MR measurements) and Russian Foundation for Basic Research, project No. 18-02-01152 (Hall effect study). The authors are grateful to V. N. Krasnorussky for experimental assistance and useful discussions.

-
- [1] S. Sachdev, Colloquium: Order and quantum phase transitions in the cuprate superconductors, *Rev. Mod. Phys.* **75**, 913 (2003).
- [2] P. A. Lee, N. Nagaosa, and X.-G. Wen, Doping a Mott insulator: Physics of high-temperature superconductivity, *Rev. Mod. Phys.* **78**, 17 (2006).
- [3] T. Timusk and B. W. Statt, The pseudogap in high-temperature superconductors: an experimental survey, *Rep. Prog. Phys.* **62**, 61 (1999).
- [4] E. W. Carlson, V. J. Emery, S. A. Kivelson, and D. Orgad, in *The Physics of Conventional and Unconventional Superconductors*, edited by K. H. Bennemann and J. B. Ketterson (Springer, Berlin, 2003).
- [5] M. R. Norman, D. Pines, and C. Kallin, The pseudogap: friend or foe of high T_c ?, *Adv. Phys.* **54**, 715 (2005).
- [6] P. A. Lee, From high temperature superconductivity to quantum spin liquid: progress in strong correlation physics, *Rep. Prog. Phys.* **71**, 012501 (2008).
- [7] J. Zaanen, Quantum phase transitions in cuprates: stripes and antiferromagnetic supersolids, *Physica C* **317**, 217 (1999).
- [8] S. A. Kivelson, I. P. Bindloss, E. Fradkin, V. Oganesyan, J. M. Tranquada, A. Kapitulnik, and C. Howald, How to detect fluctuating stripes in the high-temperature superconductors, *Rev. Mod. Phys.* **75**, 1201 (2003).
- [9] A. Damascelli, Z. Hussain, and Z. X. Shen, Angle-resolved photoemission studies of the cuprate superconductors, *Rev. Mod. Phys.* **75**, 473 (2003).
- [10] T. Yoshida, X. J. Zhou, D. H. Lu, S. Komiyama, Y. Ando, H. Eisaki, T. Kakeshita, S. Uchida, Z. Hussain, Z.-X. Shen, and A. Fujimori, Low-energy electronic structure of the high- T_c cuprates $\text{La}_{2-x}\text{Sr}_x\text{CuO}_4$ studied by angle-resolved photoemission spectroscopy, *J. Phys.: Condens. Matter* **19**, 125209 (2007).
- [11] Ø. Fischer, M. Kugler, I. Maggio-Aprile, C. Berthod, and C. Renner, Scanning tunneling spectroscopy of high-temperature superconductors, *Rev. Mod. Phys.* **79**, 353 (2007).
- [12] E. Demler, W. Hanke, and S.-C. Zhang, $\text{SO}(5)$ theory of antiferromagnetism and superconductivity, *Rev. Mod. Phys.* **76**, 909 (2004).
- [13] M. Ogata and H. Fukuyama, The $t-J$ model for the oxide high- T_c superconductors, *Rep. Prog. Phys.* **71**, 036501 (2008).
- [14] M. Vojta, Lattice symmetry breaking in cuprate superconductors: stripes, nematics, and superconductivity, *Adv. Phys.* **58**, 699 (2009).
- [15] J. M. Tranquada, B. J. Sternlieb, J. D. Axe, Y. Nakamura, and S. Uchida, Evidence for stripe correlations of spins and holes in copper oxide superconductors, *Nature (London)* **375**, 561 (1995).
- [16] C. Stock, W. J. L. Buyers, R. Liang, D. Peets, Z. Tun, D. Bonn, W. N. Hardy, and R. J. Birgeneau, Dynamic stripes and resonance in the superconducting and normal phases of $\text{YBa}_2\text{Cu}_3\text{O}_{6.5}$ ortho-II superconductor, *Phys. Rev. B* **69**, 014502 (2004).
- [17] H. A. Mook, P. Dai, F. Dogan, and R. D. Hunt, One-dimensional nature of the magnetic fluctuations in $\text{YBa}_2\text{Cu}_3\text{O}_{6.6}$, *Nature (London)* **404**, 729 (2000).
- [18] M. R. Koblishka, M. Winter, and U. Hartmann, Nanostripe structures in $\text{SmBa}_2\text{Cu}_3\text{O}_x$ superconductors, *Supercond. Sci. Technol.* **20**, 681 (2007).
- [19] Y. Kohsaka, C. Taylor, K. Fujita, A. Schmidt, C. Lupien, T. Hanaguri, M. Azuma, M. Takano, H. Eisaki, H. Takagi, S. Uchida, and J. C. Davis, An intrinsic bond-centered electronic glass with unidirectional domains in underdoped cuprates, *Science* **315**, 1380 (2007); E. H. da Silva Neto, P. Aynajian, A. Frano, R. Comin, E. Schierle, E. Weschke, A. Gyenis, J. Wen, J. Schneeloch, Z. Xu, S. Ono, G. Gu, M. Le Tacon, and A. Yazdani, Ubiquitous interplay between charge ordering and high-temperature superconductivity in cuprates, *ibid.* **343**, 393 (2014).
- [20] T. Hanaguri, C. Lupien, Y. Kohsaka, D. H. Lee, M. Azuma, M. Takano, H. Takagi, and J. C. Davis, A checkerboard electronic crystal state in lightly hole-doped $\text{Ca}_{2-x}\text{Na}_x\text{CuO}_2\text{Cl}_2$, *Nature (London)* **430**, 1001 (2004).

- [21] S. Mori, C. H. Chen, and S.-W. Cheong, Pairing of charge-ordered stripes in (La,Ca) MnO₃, *Nature (London)* **392**, 473 (1998).
- [22] M. Rubhausen, S. Yoon, S. L. Cooper, K. H. Kim, and S. W. Cheong, Anisotropic optical signatures of orbital and charge ordering in Bi_{1-x}Ca_xMnO₃, *Phys. Rev. B* **62**, R4782 (2000).
- [23] S.-H. Lee and S.-W. Cheong, Melting of Quasi-Two-Dimensional Charge Stripes in La_{5/3}Sr_{1/3}NiO₄, *Phys. Rev. Lett.* **79**, 2514 (1997).
- [24] J. M. Tranquada, Charge stripes and antiferromagnetism in insulating nickelates and superconducting cuprates, *J. Phys. Chem. Solids* **59**, 2150 (1998).
- [25] A. M. M. Abeykoon, E. S. Bozin, W.-G. Yin, G. Gu, J. P. Hill, J. M. Tranquada, and S. J. L. Billinge, Evidence for Short-Range-Ordered Charge Stripes Far above the Charge-Ordering Transition in La_{1.67}Sr_{0.33}NiO₄, *Phys. Rev. Lett.* **111**, 096404 (2013).
- [26] Q. Wang, Y. Shen, B. Pan, Y. Hao, M. Ma, F. Zhou, P. Steens, K. Schmalzl, T. R. Forrest, M. Abdel-Hafiez, X. Chen, D. A. Chareev, A. N. Vasiliev, P. Bourges, Y. Sidis, H. Cao, and J. Zhao, Strong interplay between stripe spin fluctuations, nematicity and superconductivity in FeSe, *Nat. Mater.* **15**, 159 (2016).
- [27] R. M. Fernandes, A. V. Chubukov, and J. Schmalian, What drives nematic order in iron-based superconductors?, *Nat. Phys.* **10**, 97 (2014).
- [28] S. V. Demishev, V. N. Krasnorussky, A. V. Bogach, V. V. Voronov, N. Yu. Shitsevalova, V. B. Filipov, V. V. Glushkov, and N. E. Sluchanko, Electron nematic effect induced by magnetic field in antiferroquadrupole phase of CeB₆, *Sci. Rep.* **7**, 17430 (2017).
- [29] N. Sluchanko, A. Bogach, N. Bolotina, V. Glushkov, S. Demishev, A. Dudka, V. Krasnorussky, O. Khrykina, K. Krasikov, V. Mironov, V. B. Filipov, and N. Shitsevalova, Rattling mode and symmetry lowering resulting from the instability of the B₁₂ molecule in LuB₁₂, *Phys. Rev. B* **97**, 035150 (2018).
- [30] N. B. Bolotina, A. P. Dudka, O. N. Khrykina, V. N. Krasnorussky, N. Y. Shitsevalova, V. B. Filipov, and N. E. Sluchanko, The lower symmetry electron-density distribution and the charge transport anisotropy in cubic dodecaboride LuB₁₂, *J. Phys.: Condens. Matter* **30**, 265402 (2018).
- [31] N. B. Bolotina, A. P. Dudka, O. N. Khrykina, V. V. Glushkov, A. N. Azarevich, V. N. Krasnorussky, S. Gabani, N. Y. Shitsevalova, A. V. Dukhnenko, V. B. Filipov, and N. E. Sluchanko, On the role of isotopic composition in crystal structure, thermal and charge-transport characteristics of dodecaborides (Lu^NB₁₂) with the Jahn-Teller instability, *J. Phys. Chem. Solids* **129**, 434 (2019).
- [32] A. P. Dudka, O. N. Khrykina, N. B. Bolotina, N. Y. Shitsevalova, V. B. Filipov, and N. E. Sluchanko, An exceptionally-high diffraction quality dodecaboride LuB₁₂: Growth and single crystal structure, *J. Alloys Comp.* **692**, 535 (2017).
- [33] N. E. Sluchanko, A. N. Azarevich, A. V. Bogach, N. B. Bolotina, V. V. Glushkov, S. V. Demishev, A. P. Dudka, O. N. Khrykina, V. B. Filipov, N. Y. Shitsevalova, G. A. Komandin, A. V. Muratov, Y. A. Aleshchenko, E. S. Zhukova, and B. P. Gorshunov, Observation of dynamic charge stripes in Tm_{0.19}Yb_{0.81}B₁₂ at the metal-insulator transition, *J. Phys.: Condens. Matter* **31**, 065604 (2019).
- [34] I. Bersuker, *The Jahn-Teller Effect* (Cambridge University Press, Cambridge, 2006).
- [35] N. E. Sluchanko, Magnetism, quantum criticality, and metal-insulator transitions in RB₁₂, in *Rare-Earth Borides*, edited by D. S. Inosov (Jenny Stanford Publishing, Singapore, 2021), Chap. 4.
- [36] A. P. Dudka, O. N. Khrykina, N. B. Bolotina, and V. S. Mironov, Crystal structure of dodecaborides: complexity and simplicity, in *Rare-Earth Borides*, edited by D. S. Inosov (Jenny Stanford Publishing, Singapore, 2021), Chap. 3.
- [37] See Supplemental Material at <http://link.aps.org/supplemental/10.1103/PhysRevB.103.035117> for the details of the LuB₁₂ crystal growth and characterization (Figs. S1 and S2 and Table 1); comparison of the amplitude of the resistivity and the Hall resistivity anomalies on the angular dependencies (Fig. S3); magnetic field dependencies of the reduced Hall resistivity ρ_H/H , resistivity, and Hall mobility in LuB₁₂ for samples 2 and 3 (Figs. S4 and S5); liquid helium angular dependencies of resistivity in sample 5 of LuB₁₂ (Fig. S6); the comparison of the reduced Hall resistivity angular dependencies for samples 1, 2, and 3 of LuB₁₂ (Figs. S7 and S8); the separation of the ordinary (cosin-type) and anomalous components in the reduced Hall resistivity for sample 2 of LuB₁₂ (Figs. S9 and S10); the hole-type Fermi surface sheet in LuB₁₂ (Fig. S11); quantum oscillations of resistivity and the reduced Hall resistivity in LuB₁₂ (sample 1a) (Fig. S12); and a schematic view of the ferrodistorptive effect in the RB₁₂ lattice (Fig. S13).
- [38] A. V. Rybina, K. S. Nemkovski, P. A. Alekseev, J. M. Mignot, E. S. Clementyev, M. Johnson, L. Capogna, A. V. Dukhnenko, A. B. Lyashenko, and V. B. Filippov, Lattice dynamics in ZrB₁₂ and LuB₁₂: *Ab initio* calculations and inelastic neutron scattering measurements, *Phys. Rev. B* **82**, 024302 (2010).
- [39] B. P. Gorshunov, E. S. Zhukova, G. A. Komandin, V. I. Torgashev, A. V. Muratov, Y. A. Aleshchenko, S. V. Demishev, N. Y. Shitsevalova, V. B. Filipov, and N. E. Sluchanko, Collective infrared excitation in LuB₁₂ cage-glass, *JETP Lett.* **107**, 100 (2018).
- [40] H. Harima, A. Yanase, and T. Kasuya, Energy band structure of YB₁₂ and LuB₁₂, *J. Magn. Magn. Mater.* **47**, 567 (1985).
- [41] H. Harima, N. Kobayashi, K. Takegahara, and T. Kasuya, Band calculations with occupied 4f electrons, *J. Magn. Magn. Mater.* **52**, 367 (1985).
- [42] M. Heinecke, K. Winzer, J. Noffke, H. Kranefeld, H. Grieb, K. Flachbart, and Y. B. Paderno, Quantum oscillations and the Fermi surface of LuB₁₂, *Z. Phys. B: Condens. Matter* **98**, 231 (1995).
- [43] G. E. Grechnev, A. E. Baranovskiy, V. D. Fil, T. V. Ignatova, I. G. Kolobov, A. V. Logosha, N. Y. Shitsevalova, V. B. Filippov, and O. Eriksson, Electronic structure and bulk properties of MB₆ and MB₁₂ borides, *Low Temp. Phys.* **34**, 921 (2008).
- [44] N. E. Sluchanko, A. N. Azarevich, A. V. Bogach, I. I. Vlasov, V. V. Glushkov, S. V. Demishev, A. A. Maksimov, I. I. Tartakovskii, E. V. Filatov, K. Flachbart, S. Gabani, V. B. Filippov, N. Y. Shitsevalova, and V. V. Moshchalkov, Effects of disorder and isotopic substitution in the specific heat and Raman scattering in LuB₁₂, *JETP* **113**, 468 (2011).
- [45] P. Coleman, C. Pepin, Q. Si, and R. Ramazashvili, How do

- Fermi liquids get heavy and die?, *J. Phys.: Condens. Matter* **13**, R723 (2001).
- [46] P. Coleman, J. B. Marston, and A. J. Schofield, Transport anomalies in a simplified model for a heavy-electron quantum critical point, *Phys. Rev. B* **72**, 245111 (2005).
- [47] S. Paschen, T. Luhmann, S. Wirth, P. Gegenwart, O. Trovarelli, C. Geibel, F. Steglich, P. Coleman, and Q. Si, Hall-effect evolution across a heavy-fermion quantum critical point, *Nature (London)* **432**, 881 (2004).
- [48] A. Yeh, Y.-A. Soh, J. Brooke, G. Aeppli, T. F. Rosenbaum, and S. M. Hayden, Quantum phase transition in a common metal, *Nature (London)* **419**, 459 (2002).
- [49] J. Lin and A. J. Millis, Theory of low-temperature Hall effect in stripe-ordered cuprates: Relative phase of the charge and spin potentials, *Phys. Rev. B* **80**, 193107 (2009).
- [50] L. Xie, J. F. Ding, R. R. Guo, X. F. Sun, and X. G. Li, Interplay between charge stripes and sign reversals of Hall and Seebeck effects in stripe-ordered $\text{La}_{1.6-x}\text{Nd}_{0.4}\text{Sr}_x\text{CuO}_4$ superconductors, *J. Phys.: Condens. Matter* **23**, 365702 (2011).
- [51] D. W. Koon and T. G. Castner, Hall effect near the metal-insulator transition, *Phys. Rev. B* **41**, 12054 (1990).
- [52] W. Teizer, F. Hellman, and R. C. Dynes, Hall effect at a tunable metal-insulator transition, *Phys. Rev. B* **67**, 121102 (2003).
- [53] F. Tang, Y. Ren, P. Wang, R. Zhong, J. Schneeloch, S. A. Yang, K. Yang, P. A. Lee, G. Gu, Z. Qiao, and L. Zhang, Three-dimensional quantum Hall effect and metal-insulator transition in ZrTe_5 , *Nature (London)* **569**, 537 (2019).
- [54] N. E. Sluchanko, A. N. Azarevich, A. V. Bogach, V. V. Glushkov, S. V. Demishev, M. A. Anisimov, A. V. Levchenko, V. B. Filippov, and N. Y. Shitsevalova, Hall and transverse even effects in the vicinity of a quantum critical point in $\text{Tm}_{1-x}\text{Yb}_x\text{B}_{12}$, *JETP* **115**, 509 (2012).
- [55] K. Hagiwara, Y. Takeno, Y. Ohtsubo, R. Yukawa, M. Kobayashi, K. Horiba, H. Kumigashira, J. Rault, P. Le Fèvre, F. Bertran, A. Taleb-Ibrahimi, F. Iga, and S.-I. Kimura, Temperature dependence of Yb valence in the sub-surface of $\text{YbB}_{12}(001)$, *J. Phys.: Conf. Ser.* **807**, 012003 (2017).
- [56] A. Rousuli, H. Sato, F. Iga, K. Hayashi, K. Ishii, T. Wada, T. Nagasaki, K. Mimura, H. Anzai, K. Ichiki, S. Ueda, A. Kondo, K. Kindo, T. Takabatake, K. Shimada, H. Namatame, and M. Taniguchi, Hard x-ray photoemission study of $\text{Yb}_{1-x}\text{Zr}_x\text{B}_{12}$: The effects of electron doping on the Kondo insulator YbB_{12} , *J. Phys.: Condens. Matter* **29**, 265601 (2017).
- [57] H. Werheit, V. Filipov, K. Shirai, H. Dekura, N. Shitsevalova, U. Schwarz, and M. Armbruster, Raman scattering and isotopic phonon effects in dodecaborides, *J. Phys.: Condens. Matter* **23**, 065403 (2011).
- [58] A. Anselm, *Introduction to Semiconductor Theory*, English translation (Mir, Moscow, 1981).
- [59] I. M. Lifshits, M. Ya. Azbel, and M. I. Kaganov, *Electron Theory of Metals* (Consultants Bureau, New York, 1973).
- [60] D. Parshin, Soft-potential model and universal properties of glasses (review), *Phys. Solid State* **36**, 991 (1994).
- [61] G. M. Kalvius, D. R. Noakes, R. Wappling, A. Kratzer, E. Schreier, F. Iga, T. Takabatake, and H. Von Lohneysen, μSR spectroscopy of the Kondo insulators $\text{Lu}_{1-x}\text{Yb}_x\text{B}_{12}$, *Physica B* **312**, 210 (2002).
- [62] G. M. Kalvius, D. R. Noakes, N. Marcano, R. Wappling, F. Iga, and T. Takabatake, Dynamics of the internal field in RB_{12} ($\text{R} = \text{Er}, \text{Yb}, \text{Lu}$), *Physica B* **326**, 398 (2003).
- [63] N. E. Sluchanko, D. N. Sluchanko, N. A. Samarin, V. V. Glushkov, S. V. Demishev, A. V. Kuznetsov, G. S. Burkhanov, and O. D. Chistyakov, Hall-effect anomalies near the quantum critical point in $\text{CeCu}_{6-x}\text{Au}_x$, *Low Temp. Phys.* **35**, 544 (2009).
- [64] I. Janecek and P. Vašek, Transverse even effect and Hall effect in YBaCuO superconductor, [arXiv:cond-mat/0306560](https://arxiv.org/abs/cond-mat/0306560).
- [65] J. R. Klauder and J. E. Kunzler, *The Fermi Surface* (Wiley, New York, 1960).
- [66] A. B. Pippard, *Magnetoresistance in Metals* (Cambridge University Press, New York, 1989).
- [67] H. Liu, M. Hartstein, G. J. Wallace, A. J. Davies, M. C. Hatnean, M. D. Johannes, N. Shitsevalova, G. Balakrishnan, and S. E. Sebastian, Fermi surfaces in Kondo insulators, *J. Phys.: Condens. Matter* **30**, 16LT01 (2018).
- [68] H. Hein, C. Koeppel, U. Vetter, and E. Warkentin, in *Sc, Y, La-Lu. Rare Earth Elements: Compounds with Boron*, Springer Science & Business Media (Springer, New York, 2013), p. 103.
- [69] J. Teyssier, R. Lortz, A. Petrovic, D. Van Der Marel, V. Filippov, and N. Shitsevalova, Effect of electron-phonon coupling on the superconducting transition temperature in dodecaboride superconductors: A comparison of LuB_{12} with ZrB_{12} , *Phys. Rev. B* **78**, 134504 (2008).
- [70] D. Shoenberg, *Magnetic Oscillations in Metals* (Cambridge University Press, Cambridge, 1984).
- [71] I. M. Lifshits and V. G. Peshchanski, Galvanomagnetic characteristics of metals with open Fermi surfaces. II, *Sov. Phys. JETP* **11**, 137 (1960).
- [72] S. N. Zhang, Q. S. Wu, Y. Liu, and O. V. Yazyev, Magnetoresistance from Fermi surface topology, *Phys. Rev. B* **99**, 035142 (2019).
- [73] N. E. Sluchanko, A. L. Khoroshilov, A. V. Bogach, V. V. Voronov, V. V. Glushkov, S. V. Demishev, V. N. Krasnorussky, K. M. Krasikov, N. Yu. Shitsevalova, and V. B. Filippov, Magnetoresistance scaling and the anisotropy of charge carrier scattering in the paramagnetic phase of $\text{Ho}_{0.8}\text{Lu}_{0.2}\text{B}_{12}$ cage glass, *JETP Lett.* **107**, 30 (2018).
- [74] A. L. Khoroshilov, A. N. Azarevich, A. V. Bogach, V. V. Glushkov, S. V. Demishev, V. N. Krasnorussky, V. V. Voronov, N. Yu. Shitsevalova, V. B. Filippov, S. Gabani, K. Flachbart, and N. E. Sluchanko, Isosbestic point and magnetoresistance components in $\text{Ho}_{0.5}\text{Lu}_{0.5}\text{B}_{12}$, *J. Low Temp. Phys.* **185**, 522 (2016).
- [75] N. E. Sluchanko, A. L. Khoroshilov, V. N. Krasnorussky, A. V. Bogach, V. V. Glushkov, S. V. Demishev, K. M. Krasikov, N. Yu. Shitsevalova, and V. B. Filippov, Magnetic phase transitions and the anisotropy of charge carrier scattering in antiferromagnetic metal $\text{Ho}_{0.5}\text{Lu}_{0.5}\text{B}_{12}$ with dynamic charge stripes, *Bull. Russ. Acad. Sci.: Phys.* **83**, 853 (2019).
- [76] V. Krasnorussky, V. Glushkov, A. Bogach, S. Demishev, N. Shitsevalova, V. Filipov, G. Pristas, S. Gabani, K. Flachbart, and N. Sluchanko, Anomalous magnetic contributions to Hall effect in $\text{Ho}_{0.5}\text{Lu}_{0.5}\text{B}_{12}$, *Acta Phys. Polon. A* **137**, 767 (2020).
- [77] A. L. Khoroshilov, V. N. Krasnorussky, K. M. Krasikov, A. V. Bogach, V. V. Glushkov, S. V. Demishev, N. A. Samarin, V. V. Voronov, N. Yu. Shitsevalova, V. B. Filippov, S. Gabani, K. Flachbart, K. Siemensmeyer, S. Yu. Gavrilkin, and N. E. Sluchanko, Maltese cross anisotropy in $\text{Ho}_{0.8}\text{Lu}_{0.2}\text{B}_{12}$ antiferromagnetic metal with dynamic charge stripes, *Phys. Rev. B* **99**, 174430 (2019).

- [78] A. Khoroshilov, V. Krasnorussky, A. Bogach, V. Glushkov, S. Demishev, A. Levchenko, N. Shitsevalova, V. Filippov, S. Gabáni, K. Flachbart, K. Siemensmeyer, and N. Sluchanko, Anisotropy of magnetoresistance in HoB₁₂, *Acta Phys. Polon. A* **131**, 976 (2017).
- [79] K. Krasikov, V. Glushkov, S. Demishev, A. Khoroshilov, A. Bogach, V. Voronov, N. Shitsevalova, V. Filipov, S. Gabáni, K. Flachbart, K. Siemensmeyer, and N. Sluchanko, Suppression of indirect exchange and symmetry breaking in the antiferromagnetic metal HoB₁₂ with dynamic charge stripes, *Phys. Rev. B* **102**, 214435 (2020).
- [80] K. M. Krasikov, A. V. Bogach, A. D. Bozhko, V. V. Glushkov, S. V. Demishev, A. L. Khoroshilov, N. Yu. Shitsevalova, V. Filipov, S. Gabáni, K. Flachbart, and N. E. Sluchanko, Anisotropy of the charge transport in Ho¹¹B₁₂ antiferromagnet with dynamic charge stripes, *Solid State Sci.* **104**, 106253 (2020).
- [81] J. R. Klauder, W. A. Reed, G. F. Brennert, and J. E. Kunzler, Study of the fine structure of the high-field galvanomagnetic properties and the Fermi surface of copper, *Phys. Rev.* **141**, 592 (1966).